



University of Bonn

MASTER'S THESIS FOR OBTAINING THE ACADEMIC DEGREE  
„MASTER OF SCIENCE (M.Sc.)“

## **Extracting most predictive subgraphs from models of human brain connectivity**

*Author:*

Shreya Kapoor

*First Examiner:*

Prof. Dr. Thomas Schultz

*Second Examiner:*

Prof. Dr. Holger Fröhlich

*Advisor:*

Mohammad Khatami

Submitted: November 12, 2020



# Abstract

Advances in non-invasive Neuroimaging modalities have led to a growing interest in investigating the underpinnings of human cognition and neurological disorders. Analysis of human brain connectivity or the human connectome has hence become an active area of research. Computational methods based on graph theory have played a significant role in understanding the topological organisation of brain networks. Simultaneously, machine learning algorithms are now being used in Neuroimaging studies to classify diseased states in patients. In this work, we propose a method to combine the utilities of graph theoretic methods with Machine Learning classifiers in order to obtain discriminative subnetworks in the brain. The novel component of this thesis is to reduce the graphical network derived from structural brain connectivity. Subnetworks are obtained by approximating the solution to the Maximum Edge Weight Subgraph (MEWS) problem that falls into the class of NP-hard problems. This feature selection technique makes the classification results more interpretable as compared to traditional filter based methods. The experimental results from our analysis show that MEWS subgraphs can achieve 95% area under Receiver Operator Characteristics (ROC) curve for gender classification. Furthermore, it is a generalized method which is independent of the classification task and hence can be useful for discovery of disease biomarkers.



# Contents

<b>Abstract</b>	<b>iii</b>
<b>1 Introduction</b>	<b>1</b>
<b>2 Background</b>	<b>3</b>
2.1 Magnetic Resonance Imaging . . . . .	3
2.1.1 Image formation . . . . .	7
2.2 Diffusion MRI . . . . .	9
2.2.1 Diffusion Weighted Imaging . . . . .	9
2.2.2 Diffusion Tensor Model . . . . .	11
2.2.2.1 Higher order models . . . . .	13
2.2.3 Tractography . . . . .	14
2.3 Analyzing the brain as a graph . . . . .	16
2.3.1 Connectomics . . . . .	17
2.3.2 Structural Brain Connectivity . . . . .	17
2.4 Feature Selection Techniques . . . . .	18
2.4.1 Filter methods . . . . .	18
2.5 MWCS . . . . .	19
2.6 Classification . . . . .	22
2.6.1 Support Vector Classifiers . . . . .	23
2.6.2 Random Forest Classifiers . . . . .	24
2.6.3 Multilayer Perceptron . . . . .	25
<b>3 Methods</b>	<b>29</b>
3.1 Data Acquisition . . . . .	29
3.1.1 Imaging data . . . . .	29
3.1.2 Label Preparation . . . . .	32
3.2 Creating the Connectome . . . . .	33
3.2.1 Structural Image Processing . . . . .	33
3.2.2 Diffusion Image Processing . . . . .	34
3.2.3 Connectome Representation . . . . .	35
3.3 Feature representation . . . . .	36
3.3.1 Statistical Coefficients . . . . .	36

3.3.2 Exclusion of self loops . . . . .	38
3.4 Feature selection . . . . .	39
3.4.1 Baseline analysis . . . . .	40
3.4.2 Maximum Edge Weighted Subgraph . . . . .	40
3.5 Supervised Classification . . . . .	41
3.6 Visualization . . . . .	42
3.6.1 Chord Diagram . . . . .	42
<b>4 Results</b>	<b>43</b>
4.1 Preprocessing Visualization . . . . .	43
4.2 Connectome Visualization . . . . .	44
4.3 Feature Analysis . . . . .	46
4.3.1 Differences in connectivity metric . . . . .	46
4.3.2 Self loops . . . . .	48
4.4 Baseline analysis . . . . .	51
4.5 Tracing back to original features . . . . .	51
4.5.1 Solver features . . . . .	52
4.5.2 Baseline Solver comparison . . . . .	52
4.6 Model performance . . . . .	55
4.6.1 Best parameters . . . . .	58
<b>5 Discussion</b>	<b>61</b>
5.1 Connectivity features . . . . .	61
5.2 Filter method . . . . .	62
5.3 Node weights . . . . .	62
5.4 Constraining number of nodes . . . . .	63
5.5 Personality classification . . . . .	63
<b>6 Conclusion</b>	<b>65</b>
<b>References</b>	<b>67</b>
<b>Acronyms</b>	<b>75</b>
<b>Acknowledgements</b>	<b>77</b>
<b>Declaration of Authorship</b>	<b>79</b>

# List of Figures

- 2.1 figure from Mastrogiacomo et al., 2019. (a) At first the magnetic moments of the individual nuclei are oriented randomly and cancel out each other, in the presence of an external field  $B_0$  they gain a net magnetization, with the presence of the external RF pulse the phase of the net magnetization is changed and magnetic resonance is said to occur. (b) Describes process of T1 relaxation in which the net magnetization starts to align along the static magnetic field  $B_0$ . (c) Describes T2 relaxation or the dephasing of magnetization in the transverse plane. (d) Illustrates that the value of the T1 constant is the time required to achieve 63% of the longitudinal magnetization. (e) The time constant T2 is the time required for the magnetization to fall to  $1/e$  of its value. In (d) and (e) the blue lines represent tissues containing fat while the green lines represent fluids such as Cerebro-Spinal Fluid (CSF). . . . .

2.2 Image from Ridgway, 2010 summarising the reconstruction of an encoded Magnetic Resonance Imaging (MRI) signal in 2D. A 2D slice has been selected using the gradient  $G_z$ . The phase is encoded along the y direction and the frequency is encoded along the x direction. Each phase encoding step is used to populate the k-space. The number of such steps determine the number of pixels along the y direction in the reconstructed image. The relationship between the k-space points and the points in reconstructed image space is such that  $k_x = 1/x$  and  $k_y = 1/y$ . In the k-space, each line parallel to the  $k_x$  axis corresponds to a separate MRI signal. The number of such signals is the number of times the pulse sequence is repeated. The location on the x-axis determines the time during signal acquisition. Each line parallel to the  $k_y$  axis corresponds to the amplitude and duration of the phase encoding direction (gradient) at each phase encoding step (y coordinate). . . . .

2.3	Image from Dietrich et al., 2010 elucidating the technical aspects of Diffusion Weighted MRI. The RF pulse causes a phase change of the net magnetization. Introducing the diffusion gradient adds spatial dependence of phase shift on the individual magnetic moments. The molecules that have restricted diffusion do not experience the effect of the diffusion gradient, any phase change from the first gradient is reversed by the second. They tend to relax to their equilibrium state. However, molecules that undergo free diffusion experience the effects of the diffusion gradients introduced by the second RF pulse (180 degrees) and hence will undergo a total phase shift dependent on the spatial location. This shift is manifested in terms of signal attenuation. The degree of signal attenuation depends on multiple factors as shown in Eq. (2.8). . . . .	10
2.4	Image from Muller et al., 2018 depicting different types of fiber tracking techniques. Red, green and blue indicate tracts running along the x,y and z axis respectively. (a) Depicts deterministic tracking where the largest eigenvector determines the direction of progression along adjacent voxels. (b) Probabilistic tractograph is depicted, in each voxel a probability distribution function represents multiple possible diffusion directions. . . . .	15
2.5	Illustration of classification using Support Vector Machines (SVM)s. The red line represents the decision boundary between the two classes. The algorithm maximizes the margin between the boundary for separate classes. The vectors lying on the hyperplanes depicted by the blue dashed lines are called as ‘support vectors’ and are the closest vectors to the decision boundary. Based on the values obtained by solving the L.H.S of the decision boundary for each data points, they are assigned to the corresponding classes. . . . .	23
2.6	Schematic explanation of Random Forest classifier from Tahmasebi et al., 2020. The different trees represent the decision trees constructed from the bootstrapped samples. Each tree is created on the basis of the most discriminatory features, $N_x$ for a particular bootstrapped sample. The final class of the samples in the dataset is decided on the basis of majority voting. . . . .	25
2.7	(a) Visualization of an artificial neuron from Vieira et al., 2017 depicting the output as a function of weighted sum of the inputs (Eq. 2.33) (b). The artificial neural network consisting of the input layer, hidden layers and the output layer. . . . .	26

3.1 (a) Whole brain, one million streamlines tractography computed for each subject. (b) Connectivity matrix encoding DWI information. In this case, the matrix represents the number of streamlines between any two regions of interest in the $\log_{10}$ scale. (c) Different statistical measures used to represent the importance of the original features present in the dataset.(d) Ranking used to determine the most important features which are then fed to the classifier. Parallelly, the MEWS is extracted from an input graph of statistical coefficients and is fed to the classifier (e) Classification using machine learning algorithms, such as SVMs, Random Forests (RF)s and Multi Layer Perceptron (MLP)s. . . . .	30
3.2 Pipeline for creating the connectome for each subject. Two parallel workflows following data acquisition have been illustrated in this figure. The first procedure aims to extract a parcellation mask from the structural images of each subject in their native space. The second ‘parallel’ procedure generates anatomically correspondent tractograms from diffusion images. A connectome file is generated after combining the information from filtered tractograms and parcellation mask. The connectome file contains properties of the fibers that connect Region of Interest (ROI)s determined by the parcellation mask. Image from Gerhard et al., 2011. . . . .	33
3.3 Considerations for classification task. Each path along this graph represents a different possibility for a classifier to be trained on. The parameters for training the classifier are the type of feature, the target label and the feature selection technique. . . . .	37
4.1 Visualization of pipeline used to create a connectome for each subject on an axial slice (a) Five tissue segmented image visualized in grayscale. (b) A slice of a 4D image mapped in 3D using RGB encoding tissue densities, CSF as red, GM as green and WM as blue. (c) Anatomically Constrained Tractography (ACT) of one million fibers overlaid on an axial slice of the brain. (d) Visualization of the spatial location of the center of masses of different ROIs. . . . .	44

4.2 A chord plot representing the group averaged connectome for all subjects. Nodes at the end of the circle correspond to ROIs. The thickness of each edge corresponds to the number of arcs between two ROIs. The number of arcs is proportional to the number of streamlines. In this interactive visualization the selected node (middle frontal gyrus in the left hemisphere) and its corresponding edges are highlighted while the other proprieties are made transparent. Edges connecting the selected node and target nodes are colored according to the target nodes. For example, the arcs are blue colored when there are connections to the precuneus in the left hemisphere.	45
4.3 Three overlaid histograms representing the frequency of mean z-scores for different types of features. The orange histograms are for females and blue ones are for males. The y-axis represents the number of between ROI connections. . . . .	47
4.4 Baseline analysis for gender classification. The area under ROC curve (AUC) represented as a function of percentage of features. . . . .	49
4.5 Baseline analysis on the basis of personality traits using pearson correlation coefficient as a filter method. For neuroticism, there is a trend of increase in performance with only a subset of original features using all three classifiers. The trend for the MLP shows greater than 65% AUC for top 5% of features while 45% without any feature selection. Classification performance on extraversion label increases with decrease in the number of features for classification with MLP and SVC. The strongest trend seen with the SVC, the AUC increases from 50% (without feature selection) to around 67% (using top 5% of the original features). The overall trend for neuroticism and extraversion illustrates that it is useful to do some feature selection in order to predict these traits. . . . .	50
4.6 The number of edges preserved by the MEWS solver as a function of the number of nodes supplied to the parameter $m$ (Eq. 3.3). The black dots illustrate the number of edges preserved for inputs $m \in [4, 30]$ . A quadratic curve was fitted to map this trend. The red line represents the fitted model with the parameters mentioned in the figure. Using the fitted polynomial the number of edges preserved could be predicted before running the solver. This saved computational time and effort since the nature of output graphs could be predicted beforehand. . . . .	52

4.7	10 most important nodes out of 84 determined using the MEWS solver for gender classification. The edge widths represent the f-scores of and color represents the number of streamlines between the two regions. A higher number of streamlines does not directly correspond to a higher fscore. 6 of the 10 selected nodes are subcortical regions; the thalai, the pallidai, the left hippocampus and left caudate while the remaining are cortical regions. This figure depicts that gender differences might be more prominent in subcortical brain networks than cortical brain networks. . . . .	53
4.8	41 most important features, and consequently 38 nodes preserved using baseline analysis for gender classification. The edge widths represent the f-scores and color represents the number of streamlines between the two regions. This figure shows that the baseline analysis does take graph topology into account and the features selected by this technique are not informative about any patterns such as the ones inferred using MEWS solver in Fig. 4.7. . . . .	54
4.9	Comparison of AUC for gender classification on the independent test set. The performance of three classifiers Support Vector Classifier (SVC), RF and MLP on the basis of features filtered according to the solver and baseline experiments respectively. . . . .	56
4.10	Gender classification using solver and baseline for the exact same number of features selected in each case. . . . .	56
4.11	Comparison of solver and baseline for classification of personality traits. . . . .	57



# List of Tables

3.1	Acquisition parameters for the structural image acquisition from the s900 release. . . . .	31
3.2	Parameters for the acquisition of the Diffusion MRI data acquired from the Human Connectome Project (HCP). . . . .	31
3.3	Summary of personality traits for training data subjects. . . . .	32
4.1	Results for a paired samples t-test on the test set. The paired samples are the classification metrics of the data with and without the inclusion of self loops. The p values correspond to t-test of two arrays for the same classification metric constructed using methodology in subsection 3.3.2. . . . .	48
4.2	Cross validation parameters for SVC trained for gender classification. The parameters which give the best area under the curve for the use case mentioned in the section above have been presented . .	59



# 1 Introduction

One of the greatest scientific challenges in the 21<sup>st</sup> century is to understand the structure and function of the human brain. How intricate networks of cells organize themselves at different scales and give rise to behaviour, emotion and intelligence has remained an open question in neuroscience since ages. In recent years, there has been a surge of interest to understand the human brain in health and disease. Technological advances are taking humanity closer to answering the question: what makes us, us?

Research in Neuroscience has greatly benefited from advances in Neuroimaging data acquisition, analysis and retrieval. The decreasing cost of data storage and computational memory resources has lead to development of imaging standards and made wide range studies possible. Increasing efficiency and accuracy of non-invasive imaging modalities such as MRI, Computed Tomography (CT) and Positron Emission Tomography (PET) have contributed significantly towards understanding the human brain in health and disease. Among these, MRI is a popular modality due to the diversity of information that can be generated using a single scanner. Each of the four types structural MRI, task-activated functional MRI, diffusion MRI and resting state functional MRI can be used to carry out different types of research (Van Essen and Glasser, 2016).

Excitement from investigators has brought about the progress of ambitious projects such as the HCP launched in 2009 (Van Essen and Glasser, 2016). It explores the research area known as *Connectomics* (previously known as *hodology*, the study of brain's structural and functional networks. Connectomics is aimed at creating a map of the brain divided into functionally and structurally distinct areas known as parcels. Understanding the contribution of connections between regions is important for analyzing the emergent properties of brain structure and function. This framework is also important to understand defects caused due to Neurological disorders as well as emotion and cognition (Sala-Llonch et al., 2015).

Structural brain connectivity is the study of white matter tracts in the brain and can be measured using Diffusion Tensor Imaging (DTI). Functional connectivity is based on information exchange between different brain regions and can be measured using functional Magnetic Resonance Imaging (fMRI). Each of these connectivities have their own importances but DTI based structural connectivity

is of special importance in medical applications as it provides insight into anatomical connections in the brain of individual patients, and can aid precision medicine (Cociu et al., 2017).

Machine Learning has become an indispensable tool in Neuroimaging studies due to *curse of dimensionality*, the number of subjects in the study is often much lesser than the number of features. It has often been used to make predictions based on MRI scans and classify diseased states of patients. However, for the analysis of brain connectivity there is a need for the machine learning (ML) algorithm to understand the topological properties of brain organization. Generic classifiers are not well suited for graph brain networks due to their density and computational complexity. Traditional classifiers suffer from a lack of interpretability and often do not lead to results with neurobiological correspondence (Sarica et al., 2017). Hence, it is required to incorporate the advantages of graph theoretic methods and machine learning algorithms for making neurobiologically and statistically significant predictions.

## 2 Background

Non-invasive neuroimaging techniques have become indispensable tools to understand cognitive processes and neurological disease pathology. Diffusion Magnetic Resonance Imaging (dMRI) is a new type of imaging modality often used to produce highly detailed anatomical images. It is suitable for looking at soft tissues such as those in the nervous system. White matter tractography from dMRI scans enables the inference of structural connectivity patterns between brain regions. Analysis of individual differences in structural brain connectivity is relevant to understand emotion, behavior and cognition.

Individual differences in neuroimaging are often evaluated using machine learning classifiers. Classification based on neuroimaging techniques is an intricate task. It suffers from the *curse of dimensionality* and lack of interpretability. Using graph based techniques along with feature selection methods can help establish neurobiological correspondence of the decision made by a classifier.

This chapter describes the prerequisites required to understand the implementation in chapter 3. In the first few sections the technical details of imaging using MRI and dMRI will be presented. Subsequent sections give an introduction to the prior work relevant for classification based on structural brain connectivity.

### 2.1 Magnetic Resonance Imaging

MRI is a non-invasive imaging technology that can produce 3-dimensional detailed anatomical images (McRobbie et al., 2006). This technique is based on the Nuclear Magnetic Resonance (NMR) principle. NMR a physical phenomenon in which nuclei respond to a combination of a constant and a weakly oscillating magnetic field by producing a signal at their resonant frequency. The difference between the magnetic properties of different tissue types subjected to an external magnetic field are used to generate images of biological specimens. Such electromagnetic properties are used to form images since the human body is 65% water ( $H_2O$ ). Water has an innate dipole moment of  $1.84D$  and its hydrogen nuclei act like little magnets since they have an odd number of protons and non-zero net spin.

In normal conditions (Fig. 2.1.a), i.e. in the absence of an external magnetic field

the spins of the hydrogen nuclei are randomly oriented and appear to cancel out each other when observed as an ensemble. Once the external field is applied, the hydrogen nuclei exhibit their paramagnetic nature and gain a net magnetization in the direction of the external magnetic field . This magnetization is called as the longitudinal magnetization. The initial longitudinal magnetization can be represented using the following equation:

$$\vec{M}_o = \mu \vec{B}_0 \quad (2.1)$$

where  $M_0$  is the net magnetization,  $\mu$  is the magnetic permeability or the inertia of a material to get magnetized and  $B_0$  is the external magnetic field. According to Fig. 2.1.a it can be seen that the direction of  $B_0$  defines the coordinate system for the imaging experiment. The transverse plane is defined as the plane perpendicular to the direction of  $B_0$  and the magnetization in this plane is termed as the transverse magnetization. In the presence of the external static magnetic field, the individual nuclei are precessing (rotating around their axis) with a frequency known as the Larmour frequency, which can be expressed by the equation:

$$\omega_0 = \gamma B_0 \quad (2.2)$$

where  $\omega_0$  represents the frequency,  $\gamma$  represents the gyromagnetic ration and  $B_0$  the external field.

An oscillating field operating at the Larmour frequency Eq. (2.2)) is then added to the static magnetic field using an radio frequency (RF) coil. This field is termed as  $B_1$  in Fig. 2.1.a and it causes the direction of the net magnetization vector to get altered i.e. ‘flipped’ or ‘tipped’ out of alignment with  $B_0$ . The net magnetization gets tipped towards  $B_1$  with the angle of rotation termed as the flip angle. The RF pulse exerts a torque which can be mathematically expressed as:

$$\vec{\tau} = \vec{m} \times \vec{B}_1 \quad (2.3)$$

where  $\vec{m}$  represents the magnetic moment and the  $\vec{B}_1$  is the applied magnetic field. The flipping does not bring all the spins in phase with each other but causes the net magnetization to flip onto the transverse plane ( $M_{xy}$  in Fig. 2.1.a). The magnetization  $M_{xy}$  then precesses in this plane. It is important to note that the net magnetization does not precess until an external force disturbs its equilibrium position of alignment with the static magnetic field. When the magnetization precesses, magnetic resonance is said to occur.

After this, the RF pulse is switched off which causes the tissue molecules to return to their original state and is termed as the relaxation phase. The relaxation

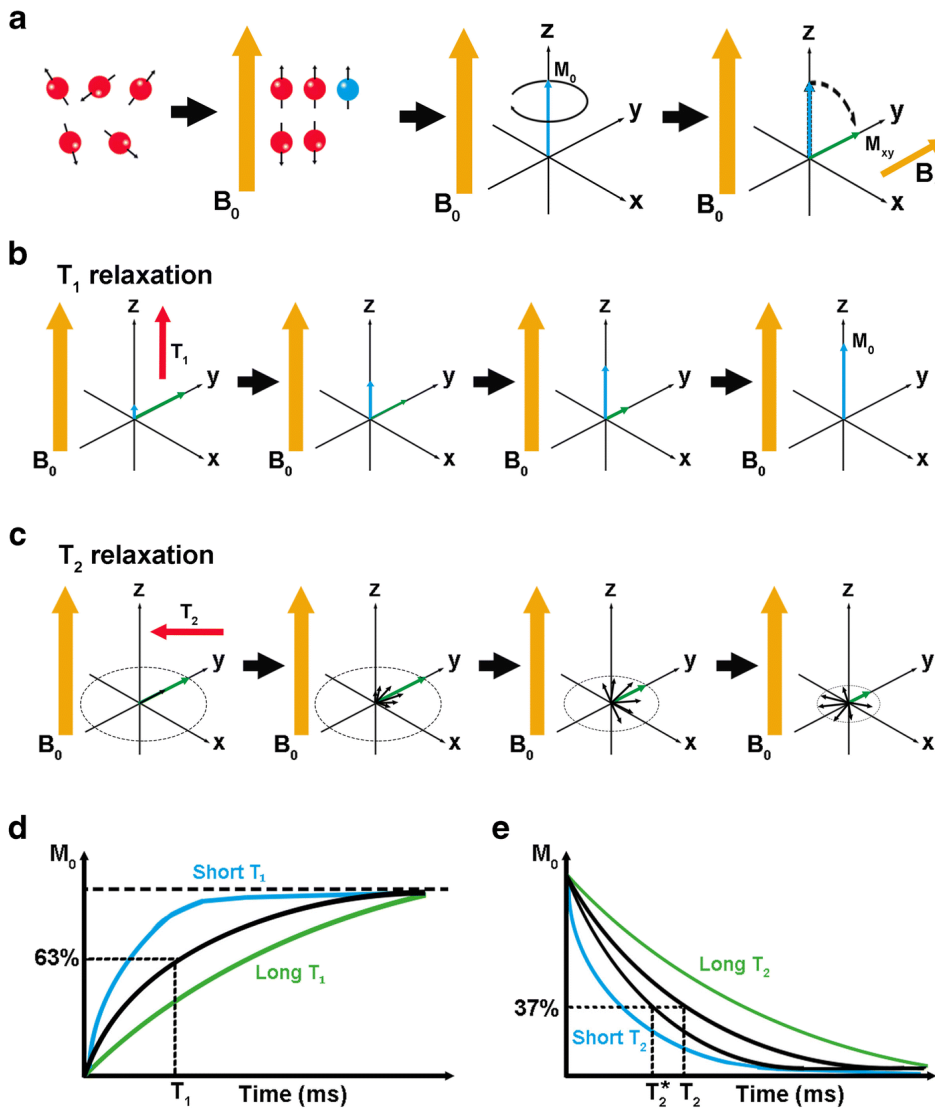


**Figure 2.1:** figure from Mastrogiacomo et al., 2019. (a) At first the magnetic moments of the individual nuclei are oriented randomly and cancel out each other, in the presence of an external field  $B_0$  they gain a net magnetization, with the presence of the external RF pulse the phase of the net magnetization is changed and magnetic resonance is said to occur. (b) Describes process of  $T_1$  relaxation in which the net magnetization starts to align along the static magnetic field  $B_0$ . (c) Describes  $T_2$  relaxation or the dephasing of magnetization in the transverse plane. (d) Illustrates that the value of the  $T_1$  constant is the time required to achieve 63% of the longitudinal magnetization. (e) The time constant  $T_2$  is the time required for the magnetization to fall to  $1/e$  of its value. In (d) and (e) the blue lines represent tissues containing fat while the green lines represent fluids such as CSF.

is due to the release of electromagnetic energy into the environment to attain thermal equilibrium. This release of electromagnetic energy is what forms the signal for the receiver coil. Bloch, 1946a introduced two time constants to measure the relaxation phase, T1 and T2.

The constant T1 measures the growth of the longitudinal component ( $M_z$ , Fig. 2.1.b) with T1 relaxation being termed as the process by which the net magnetization aligns itself along the direction of the original magnetic field. The T2 constant measures the decay of the transverse component of the magnetization (Fig. 2.1.c). The value of T2 reflects the time required for the magnetization to fall to  $\frac{1}{e}$  or 37% of its original value, illustrated in Fig. 2.1.e. Since there can be inhomogeneities inside the MRI scanner, another constant  $T2^*$  is measured as the T2 time observed while taking the recording to account for such effects. During the resonance phenomena, the magnetization has components in different directions which can be expressed in terms of the time constants and time lapse ( $t$ ) of the experiment.

$$M_x(t) = M_o e^{\frac{-t}{T_2}} \sin \omega t \quad (2.4)$$

$$M_y(t) = M_o e^{\frac{-t}{T_2}} \cos \omega t \quad (2.5)$$

$$M_z(t) = M_o (1 - e^{\frac{-t}{T_1}}) \quad (2.6)$$

Where  $M_x, M_y, M_z$  are the magnetizations along the x,y and z directions and  $M_0$  is the magnetization induced by the applied static magnetic field  $B_0$ . From Eq. (2.6) it is clear that the T1 constant measure the time required to gain the original magnetization, i.e.  $t = T1 \implies M_z = M_0$  and  $t = T2 \implies M_{xy} = \frac{M_0}{\cos \omega T2}$ . The differences in T1 and T2 times of different tissues (Fig. 2.1.d and Fig. 2.1.e) are often used to generate a contrast for image formation.

Image contrasts are indirectly controlled using repetition time (TR) and echo time (TE) in a sequence. TR is defined as the time taken between successive excitations of the same region. TE measures time between excitation and signal measurement. Short TR and short TE generate T1 weighted images while long TR and long TE generate T2 weighted images.

Different types of brain tissues have different T1 and T2 values. Short T1 times are seen in fat molecules because of their complex structure. The intricacies of saturated molecules lead to flexions and rotations which might occur at the Larmour frequency. This makes it easier for the magnetization to return to the initial state (longitudinal orientation). Longer T1 times are observed in comparatively freely diffusing mediums such as CSF. Such fluids appear dark on T1-weighted images due to longer T1 times while fat molecules appear bright with the same diffusion weighting. Fat molecules appear lighter on T2-weighted images due to short T2

time while the CSF appears bright since it has long T2 times.

### 2.1.1 Image formation

An MRI scan needs to represent the 3D nature of specimen under study. Inside an MRI scanner, the gradient coils are used to alter the magnetic field along the different spatial directions. This ensures that different slices of the biological structure to resonate at different frequencies. The signal from all the slices is then detected by receiver coils that recognize only the transverse magnetization. In neuroimaging this signal needs spatial encoding to transmit information about the millions of voxels at different spatial locations in the brain.

It is known that in order to form the 3D image the magnetic gradients are applied in the x,y,z directions. This formalism results in each voxel possessing a different Larmour frequency and the phenomenon can be termed as spatial encoding.

$$\omega = \gamma(B_0 + G(x, y, z)) \quad (2.7)$$

According to Eq. (2.7), it is evident that there is a direct relation between the gradient field and the Larmour frequency. Usually the gradient for the slice selection is applied along the z-direction. For better understanding a simpler case of 2D image reconstruction has been explained in the Fig. 2.2 where the phase encoding gradients are applied in a direction perpendicular to the frequency encoding gradients.

The RF coils in the MRI scanner detects a signal containing a mixture of frequencies specific for each slice and each phase encoding step. The distribution of frequencies is determined using a Fourier transform. This distribution is then used to fill what is called as the k-space. The 2D k-space in Fig. 2.2 is used to elucidate the components of the frequency. The intensity of a point in the space represents the contribution of the frequency  $(k_x, k_y)$  in the signal. For each combination of  $(k_x, k_y)$  in the k-space the scanner camera takes only one picture (one filter per voxel). It then estimates the actual intensities at different locations using an inverse Fourier transform. There is a one-to-one correspondence of the pixel in the k-space to the image space. Every pixel in the 2D k-space image maps to only one pixel in the reconstructed 2D image. However, it is not necessary that the locations in both the images are exactly the same. This mapping using a Fourier transform is then extrapolated in 3D in order to obtain the image of the whole organ such as the brain. Any weighting such as T1w or T2w can be given in order to generate the image after the transformation has taken place.

Another important concept for image formation is that of Field of View (FOV).

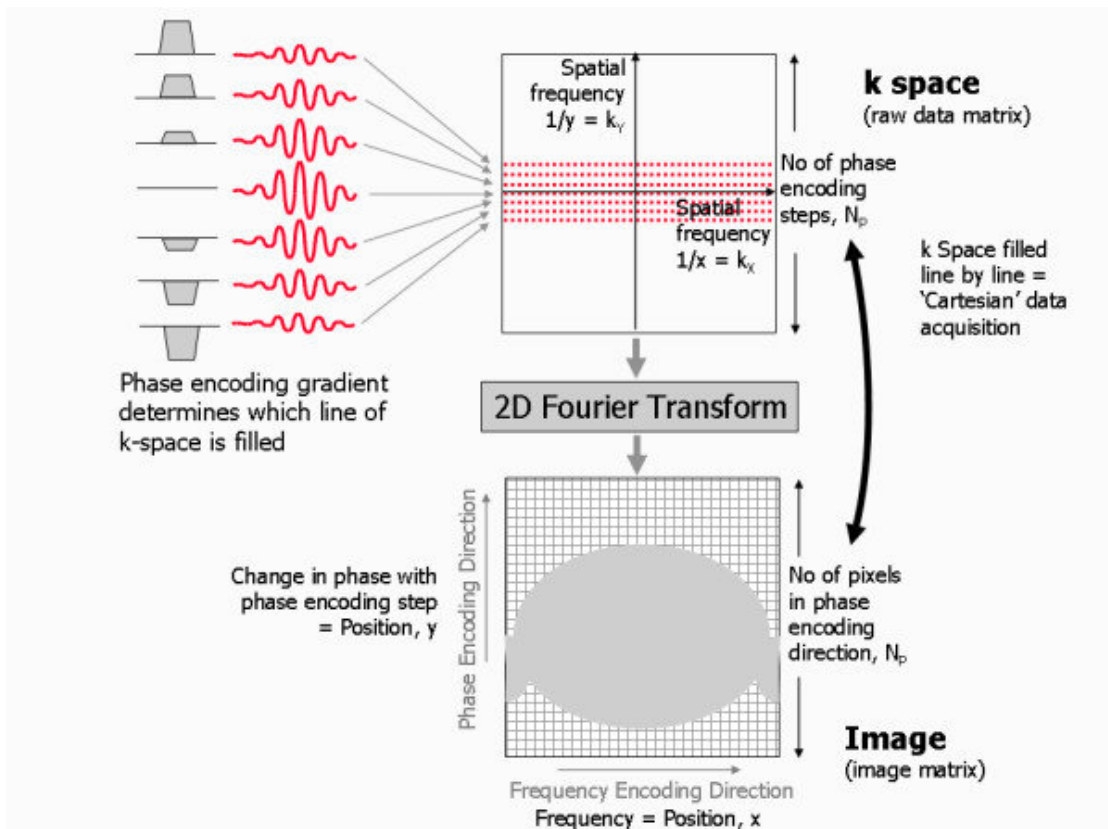


**Figure 2.2:** Image from Ridgway, 2010 summarising the reconstruction of an encoded MRI signal in 2D. A 2D slice has been selected using the gradient  $G_z$ . The phase is encoded along the y direction and the frequency is encoded along the x direction. Each phase encoding step is used to populate the k-space. The number of such steps determine the number of pixels along the y direction in the reconstructed image. The relationship between the k-space points and the points in reconstructed image space is such that  $k_x = 1/x$  and  $k_y = 1/y$ . In the k-space, each line parallel to the  $k_x$  axis corresponds to a separate MRI signal. The number of such signals is the number of times the pulse sequence is repeated. The location on the x-axis determines the time during signal acquisition. Each line parallel to the  $k_y$  axis corresponds to the amplitude and duration of the phase encoding direction (gradient) at each phase encoding step (y coordinate).

It refers to the distance over which an MRI signal is acquired or displayed. The defined FOV determines the pixel width (determined by the phase encoding y direction in Fig. 2.2) given by  $\Delta k = 1/\text{FOV}$ .

## 2.2 Diffusion MRI

dMRI is an *in-vivo*, non-invasive imaging modality that used to create high-resolution structural images of biological tissues. It measures the non-homogeneity of water diffusion in tissues to probe their microstructure (Ghosh and Deriche, 2015). One of the most important applications of dMRI is to map the white-matter fiber tracts in the brain. As compared to other MRI techniques such as fMRI it does not suffer from an issue of low resolution and low signal to noise ratio (SNR) (Wong et al., 2016).

“Diffusion” is defined as the net movement of a substance from a region of higher concentration to a region of lower concentration. In a homogeneous medium, the diffusion of water molecules is isotropic, i.e. the molecules can move in any direction with equal probability. They exhibit random walk behavior which is explained by Brownian motion (Brogoli and Vailati, 2000).

The environment inside a biological tissue is complex and the diffusion of water molecules becomes anisotropic due to the hindrances imposed by cellular membranes. This causes water molecules in the extracellular environment to experience relatively free diffusion and the ones in the intra-cellular environment experience restricted diffusion (Toennies, n.d.). This diffusion anisotropy is encoded into the MRI signal using spatial and temporal variation (gradients) in the magnetic field. This means that the alignment of the molecules is influenced by the diffusion direction. The MRI signal is said to be “Diffusion Weighted” due to signal attenuation introduced by the magnetic field gradients.

### 2.2.1 Diffusion Weighted Imaging

In Diffusion Weighted Imaging (DWI) the intensity of each voxel represents the rate of water diffusion in a cubic region. Diffusion weighting is applied in order to generate contrasts based on the assumption that diffusion varies with pathology i.e. differences in diffusion can also highlight differences in structure and function (Taylor and Bushell, 1985).

One of the most popular ways to give images diffusion weighting is by using Single-shot Spin-echo (SE) T2 weighted sequences with two symmetric gradients on each side of the 180 degree refocusing pulse. This is based on the Pulsed-gradient Spin-echo (PGSE) technique developed by Stejskal and Tanner, 1965.

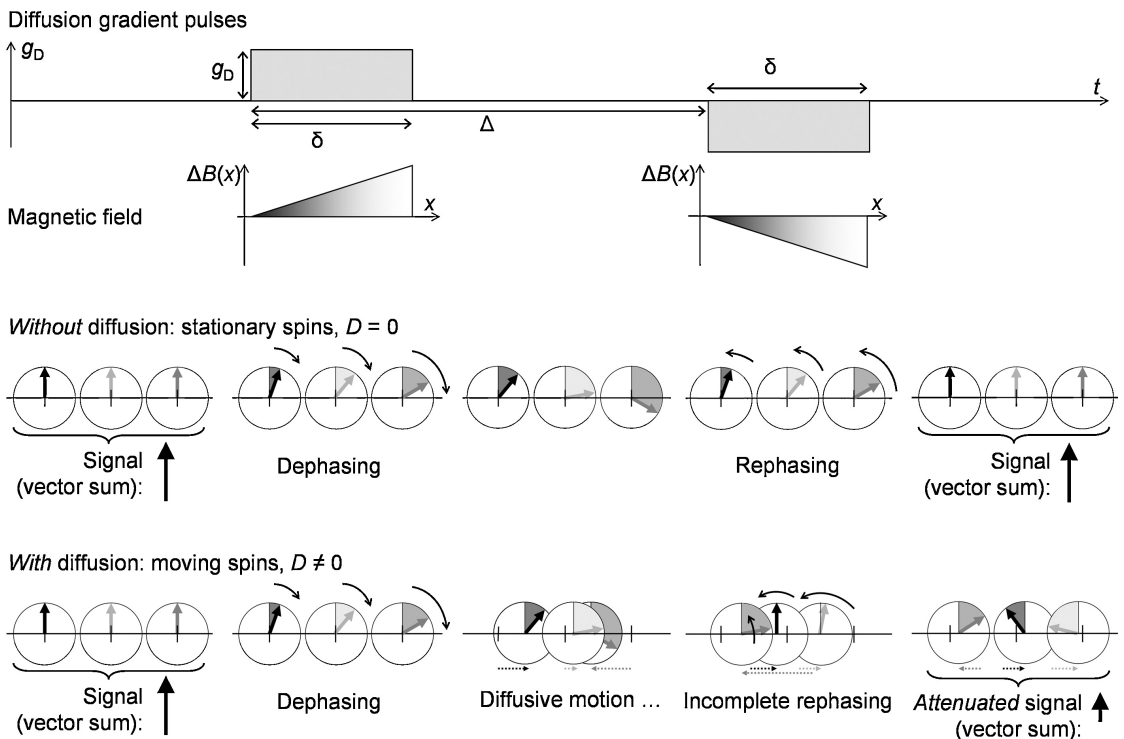


**Figure 2.3:** Image from Dietrich et al., 2010 elucidating the technical aspects of Diffusion Weighted MRI. The RF pulse causes a phase change of the net magnetization. Introducing the diffusion gradient adds spatial dependence of phase shift on the individual magnetic moments. The molecules that have restricted diffusion do not experience the effect of the diffusion gradient, any phase change from the first gradient is reversed by the second. They tend to relax to their equilibrium state. However, molecules that undergo free diffusion experience the effects of the diffusion gradients introduced by the second RF pulse (180 degrees) and hence will undergo a total phase shift dependent on the spatial location. This shift is manifested in terms of signal attenuation. The degree of signal attenuation depends on multiple factors as shown in Eq. (2.8).

PGSE improved sensitivity to diffusion in comparison to the steady state gradients used previously. Stejskal and Tanner, 1965 solved the Bloch-Torrey partial differential equations for a symmetric pair of pulsed gradients (Bloch, 1946b) and obtained the well-known Stejskal-Tanner formula:

$$S = S_0 \exp^{-bD} \quad (2.8)$$

Here  $S_0$  represents the original signal strength,  $S$  is the signal strength in a pulse sequence with the presence of diffusion gradients ( $g_D$ ) and  $D$  represents the diffusion coefficient. The attenuation of the dMRI signal by the diffusion gradients is represented in Fig. 2.3. The application of the diffusion gradient results in a spatial encoding as the Larmour frequency becomes dependent on the net magnetic field (Eq. (2.7)). In Fig. 2.3, it is evident that the Diffusion gradients are magnetic field gradients along the  $x$  direction.

Here  $\Delta B(x) = g_D x$ , which makes the Larmour frequency spatially dependent  $\Delta\omega = \gamma\Delta B(x)$  or  $\Delta\omega = \gamma g_D x$ . There is a phase shift introduced after the gradient pulse of time duration  $\delta$ . The phase shift is also dependent on the  $x$  position due to the spatial dependence represented as  $\Delta w(x)$ , the phase shift is  $\Delta\phi(x) = \Delta w\delta = \gamma g_D x \delta$ . This spatial dependence of the phase shift makes spins at different positions along the gradient axis “dephased” after the application of the gradient pulse. When the negative gradient is applied, the process of rephasing occurs. The dephasing and rephasing mechanisms result in the diffusion weighting of the image. Without any diffusion stationary spins would align along their equilibrium position (cancelling effect of the two opposing diffusion gradients) while with diffusion weighting there is a signal attenuation explained by Eq. (2.8).

The  $b$  value of the diffusion weighted signal mentioned in Eq. (2.8) is defined in the units of  $s/mm^2$  as

$$b = (\gamma g_D \delta)^2 (\Delta - \frac{\delta}{3}) \quad (2.9)$$

In order to obtain the numerical value of  $b$ , long and strong gradients are required. The diffusion gradients  $g_D$ , time of pulse  $\delta$  and time interval  $\Delta$  are often adjusted to adjust the  $b$  values. Higher  $b$  values leads to lower signal in the areas of high diffusion and increases the contrast between tissues that have different diffusion coefficients. The  $b$  values often need to be adjusted to obtain an optimal SNR.

## 2.2.2 Diffusion Tensor Model

DTI is a new type of imaging technique that relies on a tensor model to measure the diffusion on per voxel basis. Instead of attributing diffusion inside a voxel

by to a single quantity, it uses a tensor formalism to measure diffusion along different directions within a voxel. The tensor model gives a rotationally invariant description of water diffusion. With this framework DTI is hence able to trace complex fiber tracts in the brain (Jones, 2010).

DTI is a novel technology, an *in-vivo* application of DWI and is the gold standard for imaging neural fiber tracts. It has become an important brain imaging modality since various neurological disorders such as cerebral ischemia and Parkinson's disease can be attributed to white matter defects. Further, white matter constitutes about 50% of the brain (by volume) which makes it important to understand both its structure and tissue composition. Analyzing structural brain connectivity using DTI does not only help to understand the patho-physiological effect of brain disorders but also the structure of its functional networks.

In this type of imaging, each voxel is associated with a  $3 \times 3$  diffusion tensor representing the diffusion of water molecules using a Gaussian model. It is symmetric and contains six unique variables that characterize diffusion (as anisotropic or isotropic). This tensor has 3 eigenvalues and 3 corresponding eigenvectors which represent the directions of diffusion along the voxel. The voxels are usually  $1mm^3$  in size and often constitute components of more than one cell within them. The diffusion tensor can be written as:

$$D = \begin{pmatrix} D_{xx} & D_{xy} & D_{xz} \\ D_{yx} & D_{yy} & D_{yz} \\ D_{zx} & D_{zy} & D_{zz} \end{pmatrix} \quad (2.10)$$

where  $D_{xy} = D_{yx}$ ,  $D_{zy} = D_{yz}$  and  $D_{xz} = D_{zx}$ . In this case Equation 2.8 can be written as

$$\frac{S}{S_0} = \exp^{-bg^T D g} \quad (2.11)$$

where  $g^T$  is a  $3 \times 1$  unit vector representing the gradient direction. The cellular environment is heterogeneous, so water molecules in certain parts undergo free diffusion while in others they undergo restricted diffusion. Due to this restricted diffusion the measured diffusion coefficient (of the water molecules) is different from the regular diffusion coefficient of water, it is termed as the apparent diffusion coefficient (ADC). Diffusion in complex environments cannot be explained by using diffusion gradients in one direction only. Figure 2.3 shows that only the component along the gradient direction is detected. Therefore, it is required to apply diffusion gradients in three directions to get an estimate of anisotropy of water molecules. Diffusion anisotropy in a voxel means the deviation of the voxel diffusion from isotropic diffusion. High diffusion anisotropy means that there is a preferred direction for the water molecules within that voxels to diffuse (Clark

et al., 2011)

DTI images are usually represented by either encoding the tensor information using a scalar (for intensity values in a black and white image) or 4 numbers (red, green and blue (RGB) and brightness). Visually, the tensors can also be viewed as glyphs and very famously by tracing white matter tracts through a process known as tractography. The quantities such as mean diffusivity (MD) and ADC are used to characterize diffusion magnitude. Other scalars such as fractional anisotropy (FA) are used to characterize diffusion anisotropy.

MD is calculated as the trace of the diffusion tensor (Eq. 2.10). The FA determines an average ratio of diffusion distortion from the applied gradient directions. In order to calculate the FA, the diffusion tensor is converted to a diagonal matrix (which has eigenvalues D1, D2, D3 the diffusion coefficients along x,y and z directions)

$$D = \begin{pmatrix} D1 & 0 & 0 \\ 0 & D2 & 0 \\ 0 & 0 & D3 \end{pmatrix}$$

$$FA = \sqrt{\frac{3}{2} \frac{\sqrt{(D1 - D_{mean})^2 + (D2 - D_{mean})^2 + (D3 - D_{mean})^2}}{\sqrt{D1^2 + D2^2 + D3^2}}} \quad (2.12)$$

Where D1, D2, and D3 are the corresponding eigenvalues and v1,v2,v3 are the eigenvectors. DTI is a popular method to study the orientation and organisation of white matter. However, it fails in regions containing populations of fiber orientations that have different fiber orientations. It assumes that all white matter bundles in the brain have similar diffusion characteristics and attributes diffusion anisotropy to partial volume effects (J.-D. Tournier, Calamante, et al., 2004a). Secondly, the diffusion tensor only possess a single major eigenvalue for modelling the diffusion in one voxel and cannot be used for mixed fiber populations.

### 2.2.2.1 Higher order models

In order to solve the multiple fiber orientation problem of DTI mentioned in subsection 2.2.2, a number of approaches have been proposed to estimate the composition of fiber orientations inside a voxel. These models extract higher order structural information of tissues. They can help deal with problems such as kissing and crossing fibers.

High Angular Resolution Imaging (HARDI) techniques fall into the class of higher order models since they enable the detection of multi-modal diffusion sig-

nals. They include methods that incorporate the acquisition of diffusion data in more than 6 diffusion gradient directions. Q-ball imaging is one such technique but has its own limitations (J.-D. Tournier, Calamante, et al., 2004b). These methods rely on the concept of a Fiber Orientation Distribution Function (fODF). An fODF is a symmetric probability distribution function describing the distribution of fiber orientations

$$F(\Theta, \phi) = \sum_{k=1}^K w_k \delta_{\theta_k, \phi_k}(\Theta, \phi) \quad \Theta \in [0, \pi], \phi \in [0, 2\pi] \quad (2.13)$$

where  $w_k$  represents the volume fraction of each fiber passing through the voxel.  $\Theta_k$  and  $\phi_k$  represent the polar and azimuthal angles in spherical coordinates respectively.

To overcome the limitations of methods such as q-ball imaging, J.-D. Tournier, Calamante, et al., 2004a propose modelling the DWI signal as the spherical convolution (i.e. convolution in spherical coordinates) of the response function and the fODF. A response function is mathematically an axially symmetric kernel which describes the DWI signal resulting from water diffusion along each fiber bundle aligned with the z-axis in a voxel. A different response function is estimated for different fiber populations such as White Matter (WM), Grey Matter (GM) as CSF.

Spherical Deconvolution (SD) (Dell'Acqua and J.-D. Tournier, 2019) is a method in which the fODF can be extracted by deconvolving the response function from the DWI signal. Constrained Spherical Deconvolution (CSD) has also gained recent attention as a method to extract WM fiber orientation distributions as it imposes constraints to remove negative values in the reconstructed fODF. This increases the clinical feasibility and plausibility of the WM tractography (Jeurissen et al., 2014a).

### 2.2.3 Tractography

Fiber tractography is a technique used to graphically construct 3D representations of white matter pathways in the human brain. The technique uses the information about local fiber directions to trace streamlines that represent white matter tracts in the brain. It has become an important part of white matter disorder studies and has gained popularity because of its non-invasive nature. These advantages make it suitable for surgical targeting and planning (Romano et al., 2009).

Tractography methods often use DTI in order to delineate the streamlines along the white matter tracts. This is done by tracing the direction of diffusion from

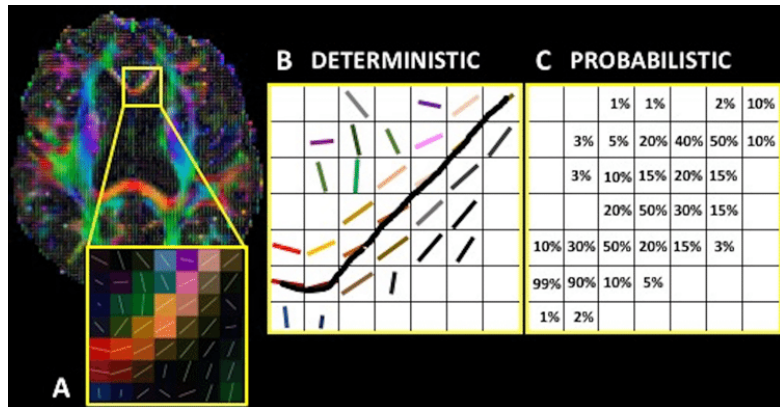


**Figure 2.4:** Image from Muller et al., 2018 depicting different types of fiber tracking techniques. Red, green and blue indicate tracts running along the x,y and z axis respectively. (a) Depicts deterministic tracking where the largest eigenvector determines the direction of progression along adjacent voxels. (b) Probabilistic tractograph is depicted, in each voxel a probability distribution function represents multiple possible diffusion directions.

one voxel to the next. Fiber tracking relies on the assumption that the direction of maximum diffusion(in the diffusion tensor) aligns with the direction of the white matter fiber within the voxel. Tractography can be divided into two classes: deterministic and probabilistic tractography.

In deterministic tractography, the algorithm usually follows the direction of maximum diffusion from along the voxels by starting from a “seed” region. If the angle between two subsequent directions of maximum diffusion is less than pre-defined threshold, the algorithm proceeds tracking along the maximum diffusion direction of the second voxel and terminates when the condition is not met (Descoteaux et al., 2008). The deterministic tractography does not take into account any random or systematic errors that arise during signal acquisition, recording and transmission.

Probabilistic tractography relies on the estimation of a probability distribution function (PDF) such as an fODF for the distribution of fiber orientations in each voxel. This helps to account for the possibility of crossing fibers and kissing fibers. The PDFs and uncertainty are then used to build a path probability map corresponding to a seed point. Let’s say  $N$  streamlines are propagated randomly from a seed point using an orientation along the distribution functions. For any two voxels

A and B

$$P_{AB} = \frac{M}{N}, \text{ probability that a curve starting at voxel A passes through voxel B}$$

$M$  = number of streamlines that go through B and A

$N$  = total number of streamlines generated from A

Using this probability map the most probable fiber orientation can be determined. From the multiple fiber orientations existing in a voxel the one most compatible with the incoming trajectory is chosen (T. E. Behrens et al., 2003).

## 2.3 Analyzing the brain as a graph

The human brain is considered to be one of the most intricate biological systems. It has been well established that this complex system can be modelled as a network composed of various dynamically interacting elements. Brain networks can hence be well represented as a graph for computational analysis. The networks perspective has gained tractable attention in neuroscience and given rise to an ever expanding field of network neuroscience. The networks of brain organization can vary at scale (from molecular interactions to cognition. With different interactions and emergent properties at each level of organization, graph theory has become an indispensable tool in this field (Sporns, 2018).

Graph theory can be defined as a branch of discrete mathematics that deals with the geometric analysis of graphs. It is useful in the analysis of biological networks since biological systems are dynamic and the interaction between the elements of the network gives rise to emergent properties. These properties can only be deciphered by comprehending network topology using a systems approach. Graph theoretic methods can give comprehensive information about brain organization, architecture, structure and function.

The wide spread application of graph theory in neuroscience has given rise to the field of *connectomics* (Sporns, Tononi, et al., 2005) for analysis of the structural and functional brain connectivity. The structural networks usually represent the anatomy of the brain and are temporally stable (ignoring effects of plasticity and development). On the other hand, the functional networks are temporally variable and dense. Structural networks are preferred when trying to study the physical nature of the brain and it's anatomy, when trying to predict Neurological disorders and searching the biochemical basis and causal relationship various factors

### 2.3.1 Connectomics

*Connectomics* is termed as the study of the brain's functional and structural networks. A connectome (in-vivo, retraced from imaging) is a dense network of brain connections, with a numerical value assigned to each network (Bassett and Sporns, 2017). The connectome of a brain can be seen as a circuit diagram with the neural connections analogous to wires and the cell bodies to electrical components.

Recently, connectomics has become the focus of major neuroscience studies. Research in the field has expanded rapidly due to the increasing interest in understanding the brain as a dynamic system, and the belief that the connections in the brain give rise to its capabilities and functionality (Sporns and Bassett, 2018).

The first complete structural connectome to be mapped at the synaptic level was published in 1986, and belongs to the species *C. elegans*. It was reconstructed using electron micrographs of serial section. It is a network that possess three hundred neurons and roughly seven thousand connections. After 1986, it still took decades to claim the biological plausibility of all the connections in the reconstructed connectome (Cook et al., 2019). This leads to the fact that the connectome of the human brain cannot be mapped using the manual labour intensive methodology used by White et al., 1986. Mapping the human brain manually hence seems implausible. The human brain contains roughly the same number of neurons as the stars in the Milky way galaxy and about  $10^{15}$  inter neuronal connections called as synapses (Fornito et al., 2015). This calls for the need to computationally determine brain connectivity from brain scans. dMRI can be used for structural connectome construction while functional MRI is the preferred modality for functional connectome construction. The HCP was launched in 2007 as the first large scale collaborative effort to create detailed maps of the brain (in-vivo) and to help better understand the fundamentals of human connectional anatomy.

### 2.3.2 Structural Brain Connectivity

Structural brain connectivity refers to the arrangement of anatomical connections in the brain. A model of the brain's structural connectivity can be derived from whole brain tractography. In organisms with complex nervous systems such as that of humans, the structural brain connectivity can be visualized at different scales. It can be either at the level of synaptic connections (microscale), at the level of neuronal populations (meso-scale) or at macro scale in which fiber tracts run between different brain regions. At all these scales, the connectivity patterns of individuals from the same species exhibit different characteristics such as organization, topology and spatial extent (Sporns, 2007).

Usually in neuroimaging studies the connectivity is analyzed at the macroscopic scale, i.e. the tracing the fibers that run in between different brain regions. From subsection 2.2.3 it can be inferred that the streamlines traced using the tractography algorithms represent the structural connections between different ROIs of the brain seen as brain nodes. The connections are usually represented using biophysical parameters such as mean FA, number of streamlines between the two nodes and the length of the streamlines connecting the two nodes.

## 2.4 Feature Selection Techniques

Neuroimaging data often suffers from the *curse of dimensionality*. The sample size is often much smaller than the total number of features. Classifiers might be influenced by the increase in noise as the number of features increases. Dimensionality reduction and feature selection are often the techniques used for a meaningful reduction in features. However, most dimensionality reduction methods such as Principal Component Analysis (PCA) rely on transformations of the original data and do not provide interpretable features. Due to this reason, it is important to consider feature selection methods where inference about which features the classifier learns can be made (Shi and Nathoo, 2018).

Feature selection methods can be grouped into three types: filter methods, wrapper methods and embedded methods. Filter methods are based on selecting features before running the classifier. Wrapper methods can be seen as a selection method *on the fly* in which features are added or removed iteratively on the basis of classification performance. Embedded methods are those in which feature selection is embedded in the classifier. All three types of methods have been increasingly used in Neuroimaging studies, however filter methods remain advantageous due to interpretability considerations (Tohka et al., 2016).

### 2.4.1 Filter methods

Filters form one of the simplest methods for feature selection. They usually serve as a pre-processing step for the classification and are model independent. However, there is a caveat to use such techniques for classification studies. Each raw feature is considered independently and their cumulative effect is not taken into consideration for the classification. Some of the common techniques used to determine the feature importance is the use of coefficients such as the f-score and t-test which are widely used in neuroimaging applications.

The f-score can be calculated as:

$$F = \frac{(\bar{x}_1 - \bar{x})^2 + (\bar{x}_2 - \bar{x})^2}{\frac{\sum_{i=1}^{n_1} (x_{1,i} - \bar{x}_1)^2}{n_1-1} + \frac{\sum_{i=1}^{n_2} (x_{2,i} - \bar{x}_2)^2}{n_2-1}} \quad (2.14)$$

where  $\bar{x}$  represents the average for all feature values,  $\bar{x}_1$  the feature average for the first class,  $n_1$  represents the number of samples for the first class and other variables follow respectively.

A simple t-test can also be computed and then the features can be filtered based on the t-statistic or the p-value to test the significance of the differences between the feature values for two different groups. Based on Inza et al., 2004, the t statistic is calculated as:

$$t = \frac{|\bar{x}_1 - \bar{x}_2|}{\sqrt{\left(\frac{\sigma_1^2}{n_1} + \frac{\sigma_2^2}{n_2}\right)}} \quad (2.15)$$

where  $\sigma_1$  represents standard deviation for the feature values of the first group and  $\sigma_2$  is the value for the second group. The features can be ranked on the basis of the p value of the t-test to obtain its statistical significance. Typically, values of  $p < 0.05$  are considered statistically significant (Colquhoun, 2017) and only then can the null hypothesis can be rejected with confidence. Numerical thresholds can also be applied for feature ranking if such a methodology is suited to the nature of the problem.

Based on a similar concept, the Pearson correlation coefficient can be used to filter features if the target variables are continuous. The Pearson correlation coefficient is defined as

$$\rho = \frac{\sum_{i=1}^N (x_i - \bar{x})(y_i - \bar{y})}{\sqrt{\sum_{i=1}^N (x_i - \bar{x})^2 \sum_{i=1}^N (y_i - \bar{y})^2}} \quad (2.16)$$

where  $y$  represents the target variable and  $N$  represents the total number of data points. This takes the linear relationship between the feature values and the target variables into account.

## 2.5 MWCS

The major aim of a Maximum Weight Connected Subgraph (MWCS) problem is to find a connected subgraph with the maximal sum of weights. MWCS problem falls into the class of NP-hard problems. This method is widely used in biological network enrichment analysis (Loboda et al., 2016). One important application of this technique is to detect differentially regulated pathways based on environmental

or phenotypical changes (Althaus et al., 2014).

The motivation to implement such a technique comes from having to process and analyze large networks. In such networks, a large number of interactions take place so it is difficult to keep a track of which one is important. It consists in identifying the biologically relevant expression changes, the "big picture" of the experiment. We need to find subnetworks important for the phenomenon we want to study. It can be extended to analyse brain networks to determine brain pathways which are correlated to a particular behavioral measurement/ physiological or epigenetic character.

This technique can also be used as a feature selection technique in order to extract the most important features from a dense graph. Consider if from a large graph a small subgraph is generated based on some correlation with another feature. Then these selected features are more important than the non-selected features for considering the feature importance in regards to a particular phenomenon. The mathematical explanation for the GMWCS will be presented in the later parts:

Consider an un-directed, connected graph  $G = (V, E)$  with weighted nodes and edges. The weighting can be both positive or negative. Let  $V$  represent its set of vertices,  $E$  the set of its nodes,  $w_e$  the weight of an edge  $e$  and  $w_v$  the weight of a node  $v$ . Mathematically, the MWCS can be described as that subgraph  $\tilde{G} = (\tilde{V}, \tilde{E})$  which maximizes the following function:

$$\Omega(\tilde{G}) = \sum_{v \in \tilde{V}} w_v + \sum_{e \in \tilde{E}} w_e \longrightarrow \max \quad (2.17)$$

The generalized MWCS can be converted into the MEWS problem for a constant number of nodes ( $m$ ). This can be done by either considering the weights of all the nodes in Eq. (2.17) as zero or equivalently constant valued so that the subgraph which maximizes the following constraint can be found.

$$\Phi(\tilde{G}) = k \times m + \sum_{e \in \tilde{E}} w_e \quad (2.18)$$

$$\Phi(\tilde{G}) = \sum_{e \in \tilde{E}} w_e \longrightarrow \max \quad (2.19)$$

According to the conceptual framework in Loboda et al., 2016, such a problem is formulated using a Mixed Integer Programming (MIP) formulation. By using a mixture of integral and binary variables, the maximal value of the objective function (Eq. 2.17) can be optimally found using a set of constraints.

The first step of formulating such a problem is to represent a candidate optimal subgraph. The membership of nodes and vertices in the subgraph is represented

using binary variables:

$$y_v = 1 \iff v \in V \text{ and } v \in \tilde{V} \quad (2.20)$$

$$w_e = 1 \iff e \in E \text{ and } e \in \tilde{E} \quad (2.21)$$

Conceptually, an edge should be present in the subgraph only if both the end vertices are also present in the subgraph. In Eq. (2.22) this condition is represented as an inequality.

$$w_e \leq y_v \quad \forall v \in V, e \in \delta_v \quad (2.22)$$

where  $\delta_v$  represents the set of incoming edges on a node. Consider if  $y_v = 0$ , then  $w_e$  has to be zero because an edge cannot be present without the node being present and if  $y_v = 1$  then  $w_e = 0$  or  $w_e = 1$  because it is not necessary for an edge to be present if a node is present.

After the subgraph can be represented, it is important to establish the validity of any subgraph. A valid MWCS needs to be connected and maximise the function Eq. (2.17). To establish the connectedness of the subgraph the concept of an arborescence needs to be introduced.

An arborescence is an acyclic directed graph in with a root node  $v$ , having exactly one path from  $v$  to any other vertex  $u$ . The connectedness in a graph is defined as the existence of a simple path between any two nodes. For creating a valid connected subgraph, its traversal has to be a valid arborescence. The MWCS is be constructed by finding a valid arborescence matching to its traversal.

The traversal of any graph can be found by considering  $S = (V, A)$  derived from  $G = (V, E)$  where each undirected edge  $(v, u)$  is replaced by two directed arcs  $(u, v)$  and  $(v, u)$ . To ensure the connectedness of the subgraph, a non-linear formulation is needed where:

- Binary variable  $x_a = 1$  iff  $a \in A$  belongs to the arborescence.
- Binary variable  $r_v = 1$  iff  $v \in V$  is the root of the arborescence,
- Continuous variable  $d_v = n$  if the length of the simple path from the root to the vertex  $v$  is  $n$ . The  $d_v$  value can be arbitrary if the vertex  $v$  does not belong to the optimal solution

As pointed above, a valid arborescence corresponds to the traversal of the connected subgraph. Hence, the arborescence needs satisfy the following constraints,

according to Haouari et al., 2013:

$$\sum_{v \in V} r_v = 1 \quad (2.23)$$

$$1 \leq d_v \leq n \quad \forall v \in V \quad (2.24)$$

$$\sum_{(u,v) \in A} x_{uv} + r_v = y_v \quad \forall v \in V \quad (2.25)$$

$$x_{uv} + x_{vu} \leq w_e \quad \forall e = (v, u) \in A \quad (2.26)$$

$$d_v r_v = r_v \quad (2.27)$$

$$d_u x_{vu} = (d_v + 1)x_{vu} \quad \forall e = (v, u) \in A \quad (2.28)$$

Equation (2.23) ensures that there is only one root of the arborescence. Equation (2.24) limits the path length from the root vertex to any other vertex in the arborescence if it is present in the subgraph. With Eq. (2.25) it can be established if a vertex is a root then there are no incoming edges and that there is a maximum of one incoming edge on each node. The constraint in Eq. (2.26) says that either the forward arc or the backward arc can be a part of the valid arborescence and not both. The last two constraints in Eqs. (2.27) to (2.28) impose that the length of the path to the root is always 1 and the distance of the nodes correspond to the direction of the edges. It can be seen that the Eqs. (2.27) to (2.28) are non-linear. Combining the above equations the linearization is as follows:

$$d_v + nr_v \leq n \quad \forall v \in V \quad (2.29)$$

$$n + d_u - d_v \geq (n + 1)x_{vu} \quad \forall (v, u) \in A \quad (2.30)$$

$$n + d_v - d_u \geq (n - 1)x_{vu} \quad \forall (v, u) \in A \quad (2.31)$$

Equation (2.29) combines Eqs. (2.23) to (2.24). Equations (2.30) to (2.31) can be justified using the fact that if a directed edge  $(v, u)$  is present, then node  $v$  is visited before node  $u$  and  $d_u - d_v = 1$ . They hence represent the Eq. (2.28). Any arbitrary node is considered to be the root of such an arborescence. The arborescence are then combined on the basis of the maximal edge and node weights to yield the final subgraph.

## 2.6 Classification

An important task in connectomics is to analyze the differences between individuals using connectivity graphs. Network based analysis rarely encompasses machine learning algorithms,

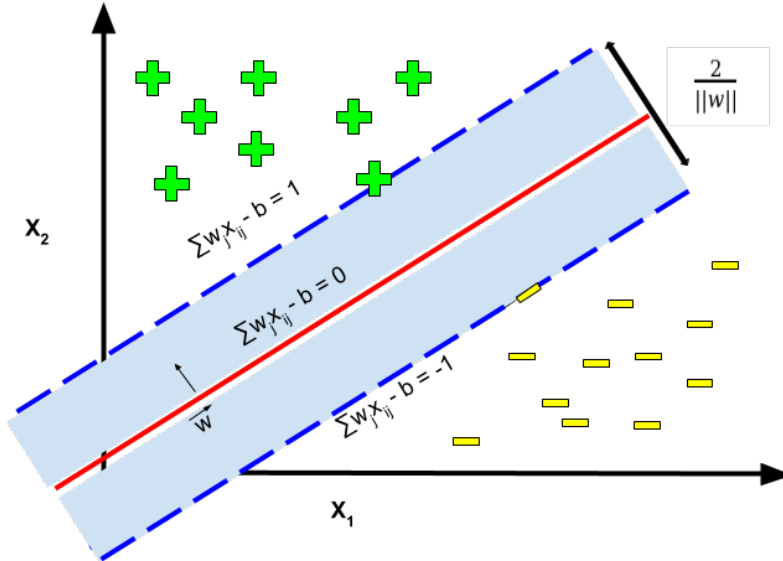


**Figure 2.5:** Illustration of classification using SVMs. The red line represents the decision boundary between the two classes. The algorithm maximizes the margin between the boundary for separate classes. The vectors lying on the hyperplanes depicted by the blue dashed lines are called as ‘support vectors’ and are the closest vectors to the decision boundary. Based on the values obtained by solving the L.H.S of the decision boundary for each data points, they are assigned to the corresponding classes.

Graph kernels are often used for classification from graphs. However, they are generalized and often not suited for problems concerning brain connectivity.

### 2.6.1 Support Vector Classifiers

SVC are classical machine learning algorithms based on SVMs. They are important since they have attained significant accuracy with different types of tasks such as a handwritten digits recognition, face detection in images, and text categorization (C. Burges and C. J. Burges, 1998). In neuroimaging studies, SVCs are important for classification tasks since they are relatively robust to overfitting and more interpretable than Deep Learning classifiers.

In the simplest, binary case the mathematical formulation of the SVM is as follows. Consider each observation  $x_i, i \in 1 \dots n$  to be a vector in the  $d$ -dimensional feature space with a target label  $y_i \in [-1, 1]$ . The classifier needs to find a boundary that separates  $n$  such points present in the presented data within a small margin of error. It does so by trying to find an optimally separating hyperplane that

efficiently divides the input data according to the target labels. In Section 2.6.1 the red line represents the optimally separating hyperplane that satisfies the equation  $\sum w_i x_i - b = 0$ . It is maximally distant to the nearest point belonging to either class (also termed as the support vectors). The maximally separating hyperplane is found by satisfying the following constraints for each data point  $i$ .

$$y_i \left( \sum_{j=1}^d w_j x_{ij} + b \right) - 1 \geq 0 \quad \forall i \in 1 \dots n \quad (2.32)$$

Here, the weights represent the parameters the model learns in order to satisfy the above conditions by solving a Langrangian equation, the mathematics of which is beyond the scope of this text.

In cases where the decision boundary is a non-linear function of the data the algorithm makes uses of what is commonly called as the 'kernel trick'. In this method the pairwise dot products of the individual  $x_i$  are replaced by a non-linear transformation or kernel function. This expression then allows the algorithm to fit the maximum margin hyperplane in the transformed space. The decision boundary is linear in the transformed space and can be projected back to find the non-linear decision boundary in the original  $d$  dimensional feature space.

## 2.6.2 Random Forest Classifiers

RF Classifiers are based on the idea of bagging or bootstrap aggregation of decision trees (Hastie et al., 2009). A decision tree is a way of recursively splitting the target variables on the basis of the rules set on the features. The name 'Random Forest' comes from the fact that the algorithm builds a 'forest' by aggregating a large number of de-correlated trees and averages them for building a classification.

The Random Forest is built in the following manner. A number of runs is specified. First, a bootstrap sample is drawn from training data. On this bootstrapped data, one tree is grown by recursively splitting the tree until the minimum node size  $n_{min}$  is reached. The steps for the recursive decision tree construction are:

- Select  $k$  variables randomly from the  $p$  total variables
- Find the most predictive variable that has the most discriminatory split point
- Split the node into daughter nodes

This method is repeated to obtain a decision tree for each time a bootstrapped sample is obtained. The individual trees are aggregated to make an ensemble

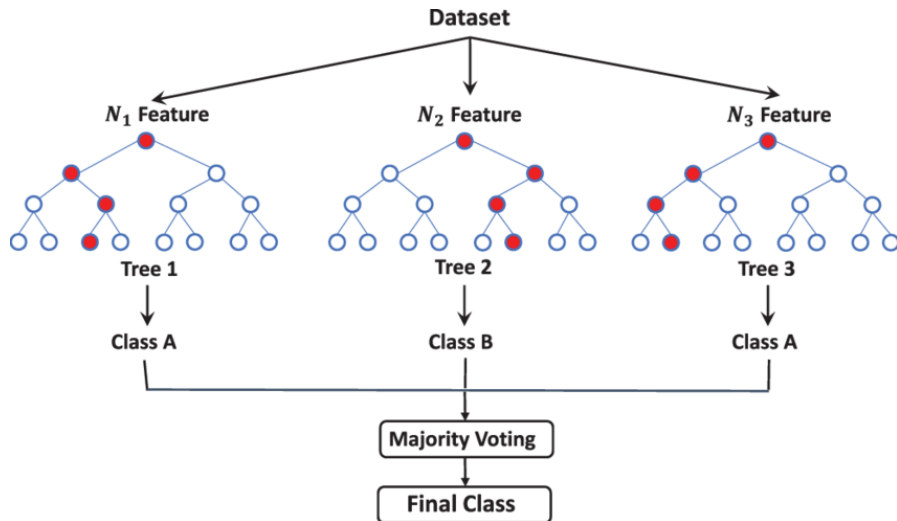


**Figure 2.6:** Schematic explanation of Random Forest classifier from Tahmasebi et al., 2020. The different trees represent the decision trees constructed from the bootstrapped samples. Each tree is created on the basis of the most discriminatory features,  $N_x$  for a particular bootstrapped sample. The final class of the samples in the dataset is decided on the basis of majority voting.

on the basis of the ensemble vote of each tree. It is evident from the Fig. 2.6, the final classification of samples is based on the majority voting and hence a feature importance can be determined. The higher the position of a split in the random forest tree, the higher is its discriminatory power. Random forest classifiers are widely used in Neuroimaging studies due to the interpretability of features which can be obtained using the feature ranking in terms of the feature importance.

### 2.6.3 Multilayer Perceptron

A MLP is an Artificial Neural Network (ANN) that is organized in the form of layers to mimic biological neural networks. The network consists of an input layer, an output layer as well as one or more hidden layers as shown in Fig. 2.7.b. Each layer consists of one or more artificial neurons (also called as perceptrons) which are connected to neurons of the subsequent layers.

The connections between the layers are feed-forward and uni-directional. The input layer serves as a buffer layer with no transformation of the input while in the other layers the neurons implement non-linear transfer functions on the weighted connections from the previous layer as shown in Fig. 2.7.a, the output  $y$  from the

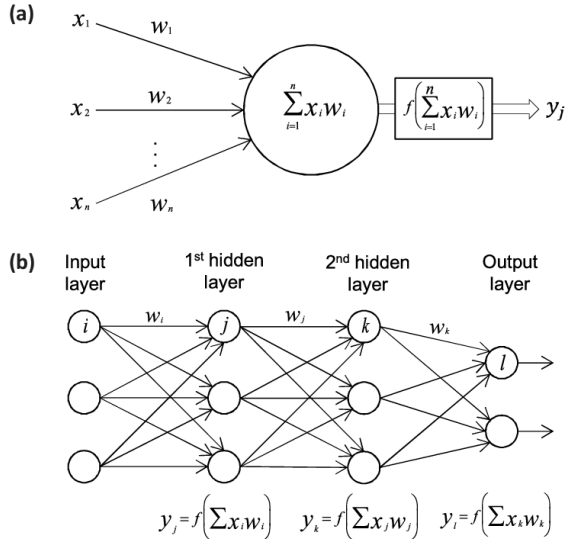


**Figure 2.7:** (a) Visualization of an artificial neuron from Vieira et al., 2017 depicting the output as a function of weighted sum of the inputs (Eq. 2.33) (b). The artificial neural network consisting of the input layer, hidden layers and the output layer.

neuron can be expressed as:

$$y = g\left(\sum_{i=1}^N w_i x_i + b\right) \quad (2.33)$$

where  $w_i$  represents the weighting of the inputs and  $b$  represents the bias for the neuron. Using the organizational structure, the neural network is able to learn complex transformations from the input data. In fact, it has been shown that an MLP with just one hidden layer and a finite number of neurons is able to act as a universal function approximator (Sifaoui et al., 2008). Consider that we have an input vector in the  $N$  dimensional space and the output is needed in the  $M$  dimensional space. An MLP (having non-linear transfer functional units) can implement any continuous mapping from the  $M$  dimensional space to the  $N$  dimensional space, with arbitrary accuracy. However, the number of neurons in the hidden layer required to achieve sufficient accuracy might be large which makes the network difficult to train.

In order to achieve better accuracy and learn hierarchical representations, the network can be made ‘deep’ by adding additional hidden layers (Bengio and Delalleau, 2011). Shallow neural networks do not generalize well unless they are given a large number of samples to train on. It is employed in neuroimaging studies in use-cases where there is a requirement to eliminate the need for manual feature

selection.



# 3 Methods

A classification task was designed for the MRI data from the HCP. The pipeline was designing this classification task consisted of four major steps. First, a whole brain tractography was generated on the basis of DWI scans for each subject. Second, three types of connectomes were created for each subject and represented in the form of connectivity matrices. Thirdly, two different feature selection techniques were deployed for classification of subjects based on the connectivity matrices. Finally, machine learning classifiers were used to test the effectiveness of these two feature selection techniques. The summary of the pipeline is presented in Figure 3.1.

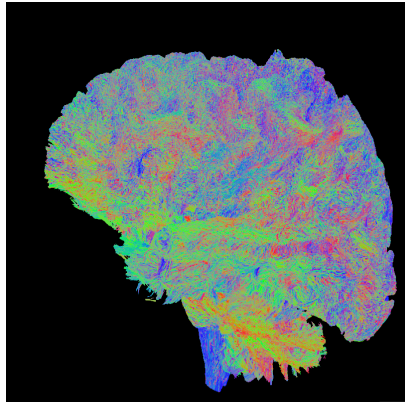
The implementation of this pipeline was scripted in *Python*. The preprocessing of the HCP data to generate tractography was done with the help of *MRtrix3* (J.-D. Tournier, R. Smith, et al., 2019). Data was prepared in a classification ready format using *Pandas* (McKinney et al., 2011) dataframes. The Maximum Edge Weight Subgraph problem was implemented in Java based on a modification from Loboda et al., 2016 ([github.com/ctlab/gmwcs-solver](https://github.com/ctlab/gmwcs-solver)). The final classification was based on machine learning from *scikit-learn* (Pedregosa et al., 2011).

## 3.1 Data Acquisition

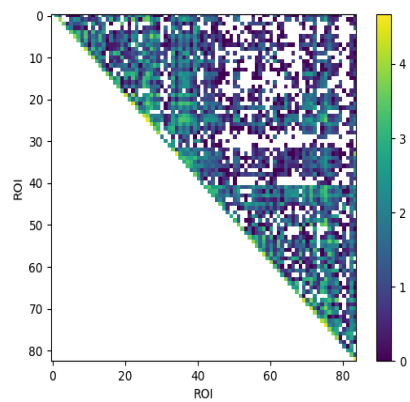
Structural and dMRI data for 203 subjects was acquired from the s900 release of the HCP (HCP, 2015). Out of the total, 101 subjects were females and 102 were males. 83 females and 58 males were aged 26-30 and remaining 34 males and 28 females were aged 22-25. The demographic information along with other markers of emotion and cognition were obtained from the unrestricted access data available on <https://db.humanconnectome.org/>.

### 3.1.1 Imaging data

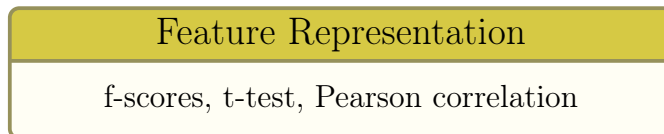
The structural and dMRI files used for this project were obtained from the repositories containing images preprocessed using version 3 of the preprocessing pipelines in the HCP detailed in Glasser et al., 2013. A Siemens 3T Skyra system was used



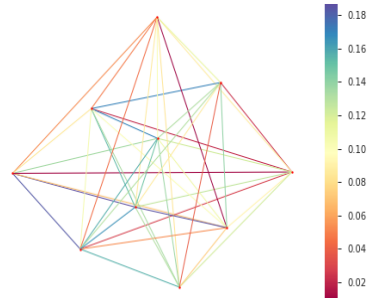
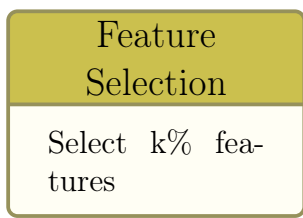
(a) Tractography



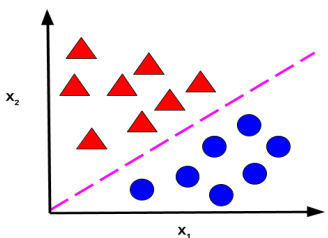
(b) Connectome



(c)



(d) Parallel feature selection using baseline analysis and MEWS



(e) Classification

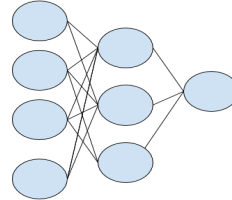


**Figure 3.1:** (a) Whole brain, one million streamlines tractography computed for each subject. (b) Connectivity matrix encoding DWI information. In this case, the matrix represents the number of streamlines between any two regions of interest in the  $\log_{10}$  scale. (c) Different statistical measures used to represent the importance of the original features present in the dataset.(d) Ranking used to determine the most important features which are then fed to the classifier. Parallelly, the MEWS is extracted from an input graph of statistical coefficients and is fed to the classifier (e) Classification using machine learning algorithms, such as SVMs, RFs and MLPs.

TR (ms)	2400
TE (ms)	2.14
T1 (ms)	1000
Flip angle	8 deg
FOV	224 x 224
Voxel Size	0.77 mm isotropic

**Table 3.1:** Acquisition parameters for the structural image acquisition from the s900 release.

Sequence	Spin-echo EPI
slice thickness	1.25 mm, 1.25 mm isotropic voxels
TR (ms)	5520
TE (ms)	89.5
Flip angle	78 deg
Refocusing flip angle	180 deg
FOV	224 x 224
Voxel Size	0.77 mm isotropic
b-values	100,2000 and 3000 $s/mm^2$

**Table 3.2:** Parameters for the acquisition of the Diffusion MRI data acquired from the HCP.

used to scan all subjects (starting in August 2012, housed at Washington University, St. Louis). The details of the acquisition protocol are can be obtained from Van Essen, Ugurbil, et al., 2012.

In order to accomplish the goals of this project, there were two types of structural image data acquired for each subject from the HCP pipeline. The first type was an image consisting of a segmentation volume along with cortical surface parcellation based on the Desikan Killiany Atlas (Desikan et al., 2006). The second type was the T1w scan in subject space. This anatomical images was aligned to the location at the interface of hemispheres: anterior and posterior commissure (AC-PC). This AC-PC alignment is a rigid body rotation so that the image gets ‘centered’ and can be termed as registration. The image was sampled at the same resolution as the diffusion data (1.25 mm isotropic, originally 0.77 mm isotropic). The parameters of the T1w images are presented in Table 3.1.

### 3.1.2 Label Preparation

The generalized pipeline implemented in this work could be used with different types of variables. Results for the big5 personality traits and gender are presented in the results section. Each of these labels were dealt with in a different manner.

The big5 personality traits are continuous. The statistical of the personality traits for the training subjects is represented in Table 3.3. Personality traits are based on the five factor model of personality (Costa Jr and McCrae, 1992). The five different personality traits are agreeableness, conscientiousness, neuroticism, extraversion and openness. They are often used in psychology and psychiatry to characterize behavior.

Statistic	Agreeable-ness	Openness	Conscientiousness	Neuroticism	Extraversion
count	141.0	141.0	141.0	141.0	141.0
mean	32.482	28.326	35.262	16.965	30.766
std	5.144	6.021	5.615	8.046	5.918
min	13.0	12.0	21.0	0.0	18.0
25%	30.0	25.0	31.0	12.0	27.0
50%	33.0	28.0	36.0	17.0	31.0
75%	36.0	32.0	39.0	21.0	34.0
max	44.0	43.0	47.0	43.0	46.0

**Table 3.3:** Summary of personality traits for training data subjects.

The architecture of the pipeline of this work required the conversion of the continuous label prediction to a classification task. The conversion steps were as follows:

1. Record the median of the personality trait the training subjects
2. Divide the personality labels into 5 quartiles
3. Remove the data of the subjects whose personality traits fall into the middle quartiles
4. Binarize the variables such that the first two quartiles belong to the lower class and the last two quartiles correspond to the higher class

The gender variables were categorical. For the classification task, male attribute was mapped to zero and females to one.

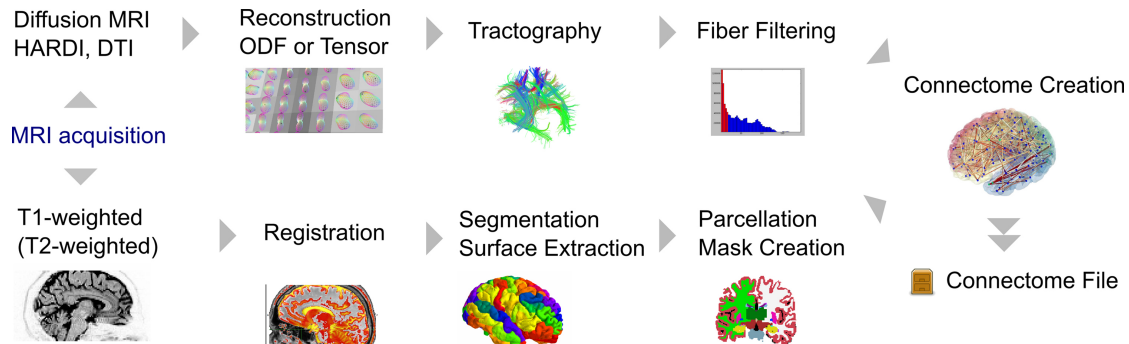


**Figure 3.2:** Pipeline for creating the connectome for each subject. Two parallel workflows following data acquisition have been illustrated in this figure. The first procedure aims to extract a parcellation mask from the structural images of each subject in their native space. The second ‘parallel’ procedure generates anatomically correspondent tractograms from diffusion images. A connectome file is generated after combining the information from filtered tractograms and parcellation mask. The connectome file contains properties of the fibers that connect ROIs determined by the parcellation mask. Image from Gerhard et al., 2011.

## 3.2 Creating the Connectome

A connectome for each subject was generated on the basis of tractography and nodes determined using a parcellation mask as illustrated in subsection 2.3.1. This workflow was implemented on the basis of the tutorial titled “ISMRM tutorial - Structural connectome for Human Connectome Project (HCP)” (<https://mrtrix.readthedocs.io/en>). The preparation of the structural connectivity matrices can be visualized in Fig. 3.2. The subsequent subsections will explain the two parallel procedures for structural and diffusion images separately.

### 3.2.1 Structural Image Processing

The first three steps of the structural image processing in Fig. 3.2 were readily accomplished by the HCP preprocessing pipeline (Glasser et al., 2013). The T1w images were registered using AC-PC alignment. In addition to creating the parcellation mask, a Five Tissue Type (5TT) segmented image was also generated. This was done on the basis of the T1w structural volume mentioned in section 3.1 sampled at the same resolution as the diffusion data (1.25 mm isotropic). The 5TT image contained differentiation of brain regions into five tissue types; namely gray matter, subcortical gray matter, WM, cerebrospinal fluid (CSF) and optionally pathological tissue. The segmentation is based on FSL segmentation tools FIRST and FAST. This information about the location of different tissue types

makes the tracking based on DWI images suitable for ACT (R. E. Smith et al., 2012). The parcellation image was used to generate a volume delineating locations of the nodes of the connectome for each subject while the T1w image in a subject's native space were used to generate a 5TT segmented image.

The segmentation surface containing the estimates of subcortical gray matter was available from the HCP data as mentioned in section 3.1. This segmentation surface was labelled according to FreeSurfer's default subcortical segmentation consisting of 9 regions, namely: caudate, pallidum, hippocampus, lateral ventricle, putamen, amygdala, thalamus, nucleus accumbens and the cerebellum. The parcellation was based on FreeSurfer's automatic surface parcellation using the Desikan-Killiany atlas that delineates 35 ROIs. The combined parcellation and segmentation image was available from the HCP data.

FreeSurfer's default lookup table for the labels of ROIs was not linear. The nodes of the original annotation image were then mapped to the default lookup table in *MRtrix3*. This made the numbering of the ROIs (also the nodes of the connectome) start from 1. Furthermore, FreeSufer's estimates of sub-cortical grey matter structures with the estimates from FSL's FIRST tool. This lookup table there were 8 subcortical gray matter regions (the accumbens area was incorporated into thalamus label) and remaining 34 ROIs were cortical gray matter regions. The structural and diffusion images available within the HCP data were used to prepare the data for probabilistic whole-brain tractography (Parker et al., 2003).

### 3.2.2 Diffusion Image Processing

For this project, the structural images from subject's native space were taken due to the nature of the tractography. Tractography is performed in the subject space since a structural image in this space is the best approximation of the subject's physical brain. The important characteristics of the dMRI images acquired is that they obtained in very high resolution (1.25 mm isotropic) using a Stejskal-Tanner (monopolar) diffusion encoding scheme as mentioned in Figure 2.2.1. The q-space was sampled by including 3 shells at the b-values presented in Table 3.2 with each gradient table defined by a single b-value acquired once with right-to-left and another in the opposite phase encoding polarities.

For each subject, four types of DWI files were used:

- Preprocessed diffusion time series
- Brain mask in diffusion space
- Diffusion weighting for each volume

- Diffusion direction for each volume

The first step of processing the diffusion images is to determine the fODF for probabilistic tractography. The fODFs were reconstructed using multi-shell, multi-tissue constrained spherical deconvolution (MSMT-CSD) based on the algorithm in Jeurissen et al., 2014b. As mentioned in subsubsection 2.2.2.1 the CSD of response functions can determine the fODF distribution. Hence, CSD of the separate response functions from WM, GM and CSF was done in order to obtain the DWI signals of the three tissue types from the 5TT image.

The probabilistic whole-brain tractography of five-million fiber tracts was generated using ***MRtrix3***. The streamlines were computed on the basis of the algorithm iFOD2 (J. D. Tournier et al., 2010). This algorithm uses the fODF image and determines candidate streamline paths (arcs), which have greater fODF amplitudes along the paths. By sampling the underlying fODF amplitudes along these arcs , it makes the streamlines likely to follow most probable paths.

Anatomical constraints on the tractography were provided using the 5TT image. There were other series of constraints imposed in order to make the tractography more informed. The seed points were dynamically determined using the Spherical Informed Filtering (SIFT) model R. E. Smith et al., 2013 of the white matter fODFs. The cutoff value of 0.06 was set for FOD amplitude for terminating tracks. The maximum length of streamlines was set at 250 mm (200 times the voxel size) when the voxel size is 1.25mm. The tracking along a streamline was truncated if the fiber terminates at poor structural, then retracking is performed. The streamlines were cropped whenever as the streamlines cross the grey matter-white matter interface.

The tractography was then downsampled from five million fibers to one million fibers to preserve the most biologically relevant fibers using the SIFT algorithm (R. E. Smith et al., 2013). This provided more meaningful estimates of the structural connection density and also reduced the memory requirements.

### 3.2.3 Connectome Representation

The connectome can be represented in the form of a graph as mentioned in subsection 2.3.1. After obtaining the streamline file and a parcellation image representing the subject specific node locations of the connectome, the connectome matrix was obtained in a *.csv* format. It was generated from the whole brain tractography of one million tracts using 84 relevant grey matter parcellations (in ***MRtrix3***).

The 84 nodes represent a 8 subcortical gray matter ROIs and 34 cortical gray matter ROIs with each ROI contributing to two nodes (one in the left hemisphere and another in the right hemisphere). Using different parameter settings three

types of features were extracted. The mean FA (Eq. 2.12), the average length and number of streamlines between any two regions. The visualization can be seen in the Figure 3.1b. The connectome is represented as an upper triangular matrix( $84 \times 84$ ) considering that the connections between two ROIs are symmetric.

### 3.3 Feature representation

Once the connectivity matrices for all the 201 subjects were computed and encoded in the format of a .csv file, a *pandas dataframe* was prepared to serve as input to the classifier. Each row represented the data for an individual subject. Each column represented the connection between any two brain regions i.e. features in one cell of the connectivity matrix. Three different types of features obtained using the connectome files according to subsection 3.2.3. The design of the classification task was based on different attributes presented in Figure 3.3. A classifier was trained on one set of configurations for two different feature selection techniques. The details will be discussed in the subsequent subsections.

Self-loops were omitted from the analysis pipeline due to incompatibility with the solver based implementation and non-significant changes to classification accuracy based on the omission. Furthermore, using the calculation of statistical coefficients on the raw data the importance of each feature was determined.

The training set consisted of 141 subjects consisting of 83 females and 58 males aged 26-30. While the independent test set consisted of 34 male and 28 females aged 22-25. The data was standardized using *sklearn* by removing the mean and scaling to unit variance since the different types of features were in separate scales of magnitude.

#### 3.3.1 Statistical Coefficients

The raw features were not representative of any information on a group level. To gain information about feature importance statistical coefficients were used. From the raw matrices, each column was be represented as a statistic and hence ‘group averaged’ edge of the connectivity graph.

Statistical coefficients are effective feature filter methods for the classification from Neuroimaging data. Filter methods were used since they can be retraced to the original features. Mainly, three coefficients were used. The first two were the t-test and the f-scores, which describe the discriminative power of a particular feature. The Pearson correlation coefficient was used in the case of continuous variables to capture the linear relationships between the features and the target values.

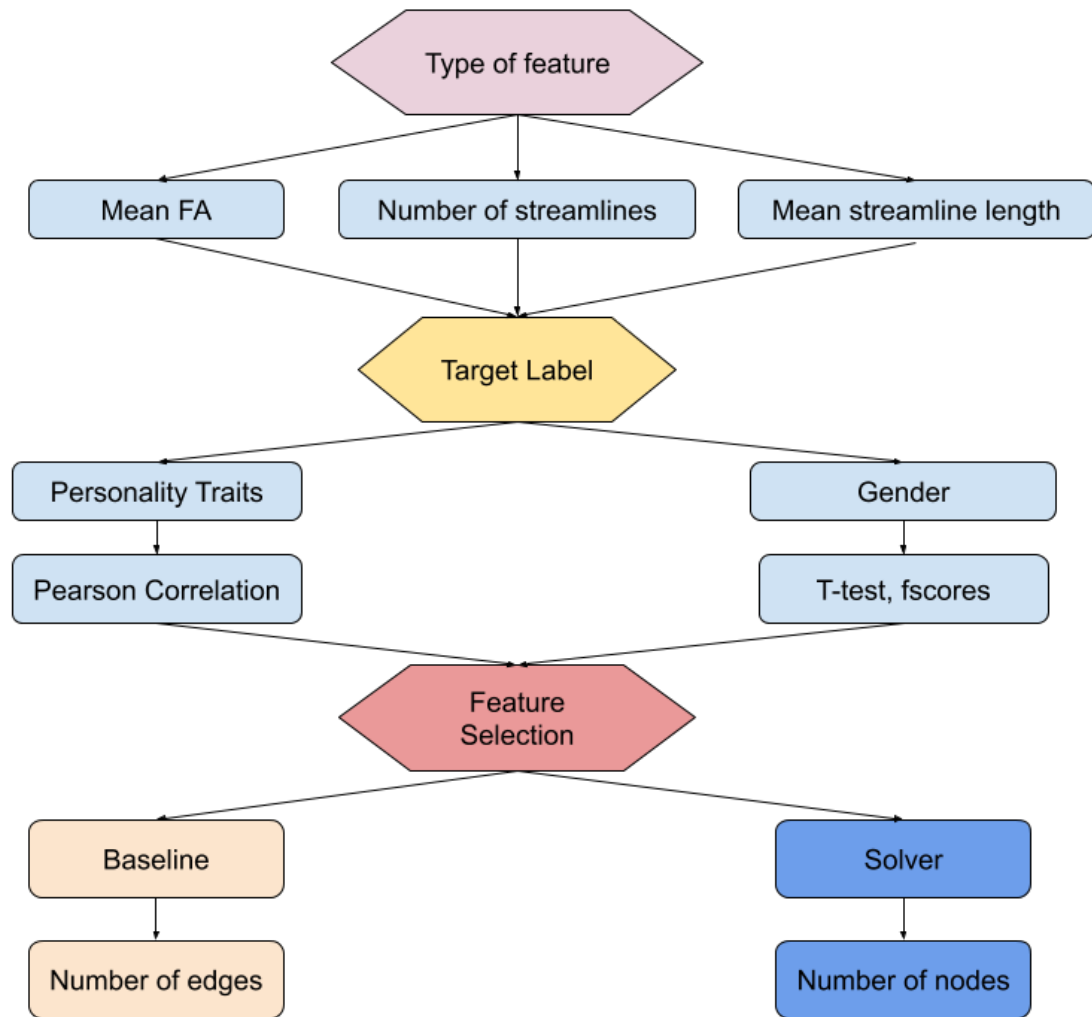


**Figure 3.3:** Considerations for classification task. Each path along this graph represents a different possibility for a classifier to be trained on. The parameters for training the classifier are the type of feature, the target label and the feature selection technique.

The f-score used in the analysis is used to measure how well the particular feature distinguishes between the two classes labelled as 1 and 2. It was calculated according to Eq. (2.14). For the Pearson correlation coefficient, the absolute values were taken.

The t-test was processed in a different manner as compared to the first two metrics, the training data was divided into two groups, one belonging to class 1 and the other belonging to class 2. The null-hypothesis remained that the means of the given feature for the two samples are identical i.e.  $\bar{x}_1 - \bar{x}_2 = 0$ . The p-value of the t-test was used to determine it's statistical significance by converting it into the  $\log_{10}$  scale. Each p-value  $p_x$  was represented by  $f(p_x) = (-1) \times \log_{10} p_x$  so that a higher numerical value represents a higher statistical significance.

### 3.3.2 Exclusion of self loops

Self loops can be termed as the connections from the brain regions to themselves. They were excluded from the analysis before feeding data to the classifier. These loops were incompatible with the MEWS implementations and hence they were removed from baseline analysis performance comparison between the two methods. Further, this exclusion will be justified by the performance of the classifiers with and without the inclusion of self-connections between the ROIs in subsection 4.3.2.

Their exclusion was an important consideration for the MEWS solver based implementation. Degenerate edges are not part of a simple graph, their inclusion was incompatible with the implementation from Loboda et al., 2016. After removing such connections the MEWS implementation was able to solve the MIP formulation and produce subgraphs.

The results in subsection 4.3.2 help evaluate the importance of self loops was ascertained by seeing their effects on classification metrics. This is done on the basis of a paired samples t-test. The first sample is taken as the classification performance on the data including the self loop features. Alternatively, the second sample is the classification performance obtained by excluding self loops. In general, the null hypothesis of a paired sample t-test remains that the differences between the observations from two samples is zero. Two slightly different experiments were carried out for classification of personality traits and gender. The formulas for calculation however remain the same. The t-statistic is calculated by:

$$t = \frac{\tilde{X}_D - \mu_0}{\frac{s_D}{\sqrt{n}}} \quad (3.1)$$

$$\tilde{X}_D = \sum_{i=1}^N \frac{a_i - b_i}{n} \quad (3.2)$$

where  $s_D$  is the standard deviation of the differences between the metrics of the experiments with the self loops  $a$  and without the self loops  $b$ . Arrays  $a$  and  $b$  have the same length  $n$ . There was one entry in the array for each possibility in a combination of choice for different attributes:

- Classification label
- Percentage of features in the set [2, 5, 10, 50, 100]
- Three different classifiers MLP, support vector machines, and random forest classifier
- Edge type (representatives of raw features, subsection 3.3.1) depending on classification label

The null hypothesis for classification of personality traits was that the average of a particular classification metric on the basis of one feature (such as mean FA, mean streamline length and number of streamlines) is the same. Including data for all five personality traits and one type of edge for arrays  $a$  and  $b$  had a size  $n = 75$  i.e.  $5 \times 5 \times 3 \times 1$ .

In a similar fashion, the null hypothesis for the gender based classification the same. However, instead of five personality traits there was one label used i.e. gender and two edge type (t-test and f-scores). This resulted in  $n = 30$  i.e.  $1 \times 5 \times 3 \times 2$ .

The null hypothesis could not be rejected because for the test data, the p-values of these t-tests were high. This indicates that the difference between the classification on the data with and without the self loops is not statistically significant. Self loops could hence be safely eliminated and the results of these experiment are presented in subsection 4.3.2.

## 3.4 Feature selection

The motivation to perform feature selection from considerations of time complexity and removal of redundant features. There were two types of feature selection

techniques used before classification. The first one a classical feature selection technique based on statistical coefficients and is termed as the ‘baseline’. The second technique is based on extracting a subgraph after converting the original edge weights to statistical coefficients and is termed as the ‘solver’ method based on the MEWS.

The MEWS technique produces more interpretable results as compared to filter methods due to incorporation of graph topology. It is proposed due to the fact that analyzing the inter-subject differences at the subnetwork level is easier than analyzing dense subgraph of whole brain connectivity.

### 3.4.1 Baseline analysis

Baseline experiments were solely based on the filter methods mentioned in subsection 2.4.1. In this technique, there is no information about graph topology or the biological correspondence of the features. Feature importance is determined purely on numerical values.

For each of the structural connections, the statistical coefficient was calculated based on the data and target variables from the training set. The metrics mentioned in subsection 3.3.1 were then used to rank the features. This ranking was based on first taking the absolute value of the coefficients and then dividing the coefficients for all features into a percentile distribution. This gave a ranking from which the top percentiles were selected according to a parameter  $k$ . Initially  $k \in \{2, 5, 10, 50, 100\}$  were chosen to cover the overall trend of classifier performance as a function number of features. Later in the course of multiple experiments this parameter  $k$  could be adjusted according to requirements for comparison to the number of features extracted by the MEWS solver.

### 3.4.2 Maximum Edge Weighted Subgraph

The special case of the (section 2.5), the MEWS was implemented because of no predefined node weighting for the regions of interest. The implementation was based on the Java application from Loboda et al., 2016. This application made use of the IBM ILOG CPLEX studio version 12.10 Java Application Processing Interface (API).

For each type of feature a separate graph was created specific to the target label of interest. The nodes in this graph consisted of a total of 84, out of which 70 are defined by the cortical gray matter parcellations based on the Desikan-Killiany Atlas and 14 are subcortical gray matter segmentations. The edges were the connections between the ROIs weighted by the statistical coefficients calculated

for the training data with respect to the target variables. Such a graph was termed as the input graph.

All nodes in the input graph were given a constant negative weighting of  $\{-0.01\}$ . This was done to ensure a negative penalty on the inclusion of an extra node. This ensured the conservation of a specified number of nodes alongside compatibility for MEWS (Eq. 2.19). Additionally, sparsity to the input graph was introduced using two constraints. The absolute value of the edge weights (raw features represented by statistical coefficients, subsection 3.3.1 shall not be zero. Simultaneously, features are conserved if and only if the tractography of each subject contains at least one streamline between the two nodes.

For creating the output graph, parts of the pipeline used in Loboda et al., 2016 were modified. Constraints mentioned in section 2.5 were extended and the additional constraint was to preserve a specified number of nodes using the constraint:

$$\sum_{v=1}^V y_v = m \quad \forall v \in V \quad (3.3)$$

where  $m$  is a controllable parameter specifying the number of nodes needed to be preserved in the output graph and  $y_v$  is the binary variable mentioned in Equation 2.20. The preprocessing module of the MCWS Java solver was disabled due to its incompatibility with the required constraint (Eq. 3.3).

An object oriented approach was taken to implement a class derived from the *networkx* (Hagberg et al., 2008) for the different input graphs and their corresponding output graphs. At any time, the graphs created for a specific use case could be read from text files and their properties could be explored.

In order compare the features selected with this technique to the baseline experiments, it was important to infer the number of edges being preserved based on a specific input configuration. The output number of edges was then analyzed as function of the number of nodes. The results are presented in Fig. 4.6.

## 3.5 Supervised Classification

A Randomized Search 5 fold cross validation with implementation from *scikit learn* was carried out for different algorithms in different cases based on the type of feature, the feature selection technique, target variables along with target labels are presented in Figure 3.3. The cross validation was refitted using balanced accuracy on the test set. After the randomized search was finished, the best estimator was taken and fit to the training set. This classifier was then used to make predictions

on an independent test set with difference in age range.

The training set consisted of 141 subjects, 83 females and 58 males aged 26-30. The independent test set consisted of 62 subjects, 34 males and 28 females aged 22-25. The different age ranges for the training and the test set were chosen in to remove the confounding factors of age. Particularly when it came to personality traits which could be influenced by the age. If the training set consisted of different age ranges the algorithm could become biased by learning the age effects.

One model was trained each time there was a different configuration of settings presented in Figure 3.3. Classification performance was assessed using the metrics area under ROC curve, f1-score, accuracy and balanced accuracy.

## 3.6 Visualization

Since the graphs included in the analysis for each subject were dense. It was important to design effective visualization techniques for intuitively interpreting the features selected by the baseline and solver based method.

### 3.6.1 Chord Diagram

A chord diagram is an effective way of visualizing the flow between different nodes. The connectome containing the feature of the number of streamlines that connect any two ROIs was represented a chord diagram created with the help of package *holoviews* (Stevens et al., 2015). Each ROI was represented as an entity or a fragment in the outer circle. The arcs drawn between the different node represent the connections and their thickness is proportional to the value of the number of streamlines in our case. In Fig. 4.2 the average number of streamlines (for all subjects) between any two regions are visualized. There are multiple arcs connecting the two regions and these arcs get bundled and result in a thicker arc.

# 4 Results

In this section, the quantitative and visualization results from the methods presented in chapter 3 will be presented. The first two sections will present results from preprocessing of the DWI images mentioned in subsection 3.2.2 and extraction of connectivity matrices. The subsequent sections will statistically describe the nature of the data as well as classification results based on the comprehensive classification parameters illustrated in Figure 3.3.

## 4.1 Preprocessing Visualization

During the process of generating the connectome (subsection 3.2.3) visual inspection was required to investigate the properties of different types of images produced. The results illustrated in Fig. 4.1 were used to evaluate the adherence of the implementation to the conceptual framework mentioned section 3.2.

The 5TT image obtained after tissue segmentation (subsection 3.2.1) was 4D and could not be easily displayed in 3D. In Fig. 4.1.a, this 4D image is displayed according to gray-scale mapping in 3D. With the grayscale mapping, it was visually observed that the 5TT images did not contain any erroneous labels. The original 4D image contained three volumes with each one representing the corresponding tissue densities of WM, GM and CSF. In Fig. 4.1.b, the 5TT 4D image is visualized as an RGB image with each volume getting its specific color, i.e. WM as blue, GM as green and CSF as red. In an interactive window from *mrview* (J.-D. Tournier, R. Smith, et al., 2019) the RGB image can be zoomed in and checked for compliance of the response functions with the fODFs and tissue segmentations.

After obtaining information about the tissue segmentations and fODFs, one million fibers whole brain tractography was generated (Fig. 4.1.c). In this tractogram, the red fibers run in right to left direction, green between anterior-posterior and blue in head-to-foot direction (Hobert et al., 2013). Finally, the connectome could be visualized (Fig. 4.1.d) with the nodes representing the center of mass of grey matter regions and edges as the connections between them. The intensity of this image is not equal to the signal intensity but the number assigned to the ROI, so any ROI that has a higher numbering in the lookup table is shown brighter.

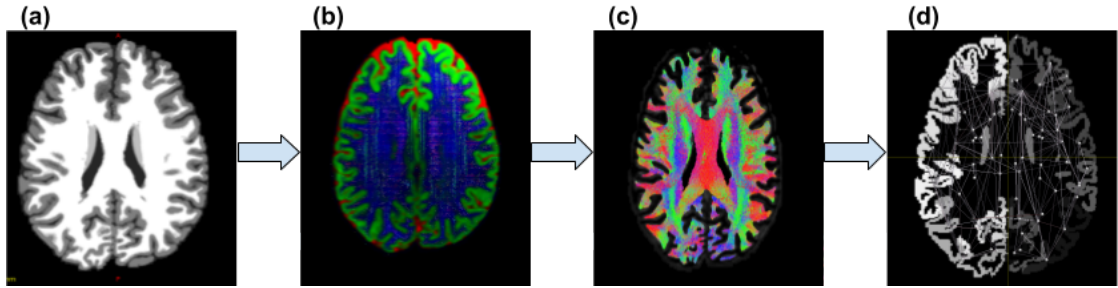


**Figure 4.1:** Visualization of pipeline used to create a connectome for each subject on an axial slice (a) Five tissue segmented image visualized in grayscale. (b) A slice of a 4D image mapped in 3D using RGB encoding tissue densities, CSF as red, GM as green and WM as blue. (c) ACT of one million fibers overlaid on an axial slice of the brain. (d) Visualization of the spatial location of the center of masses of different ROIs.

Overall, visualizing the preprocessing pipeline helped to evaluate the anatomical correspondence of the tractography. It also helps understand the relationship between the generated connectome and white matter structural brain connectivity.

## 4.2 Connectome Visualization

After the connectivity matrices for all subjects were generated using the methods in section 3.2, the group averaged connectome was created. The raw connectivity matrix was dense, containing  $n = 84$  nodes and  $n_e = 3486$  edges. The edge weights had high standard deviations for all the three connectivity metrics: mean FA, mean streamline length and number of streamlines. Visualizing the connectome as a simple connectivity matrix or a heatmap was hence not an effective strategy.

A chord plot was chosen because of the ease of representing grey matter nodes along the boundaries of the graph. The number of streamlines could also be encoded within a chord plot since the number of arcs drawn between any two nodes can be easily specified. The reason for the selection of the number of streamlines as a valid connectivity metric will be presented in subsection 4.3.1. Furthermore, the detailed coloring scheme used for creating the chord plot gives added visual cues about the source and the target nodes. Once a node is selected the edges get colored according to the color of the target node.

In the chord plot represented in Figure 4.2  $n = 65$  nodes are shown. All nodes were colored to the color palette in *holoviews*, with each node getting a different color. The graph is obtained by thresholding the group averaged number of streamlines between any two ROIs. The threshold was selected to be  $N = 900$ .

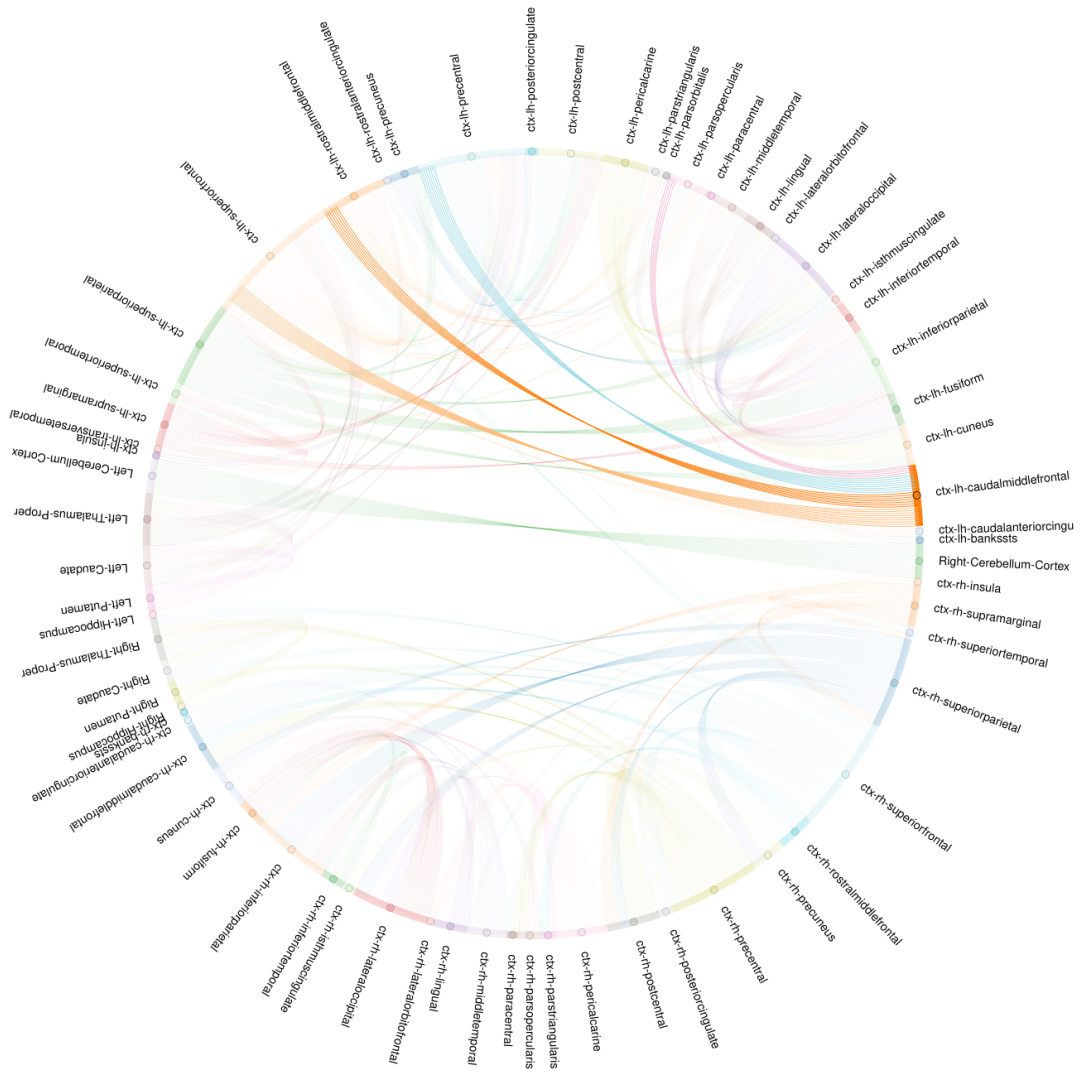


**Figure 4.2:** A chord plot representing the group averaged connectome for all subjects. Nodes at the end of the circle correspond to ROIs. The thickness of each edge corresponds to the number of arcs between two ROIs. The number of arcs is proportional to the number of streamlines. In this interactive visualization the selected node (middle frontal gyrus in the left hemisphere) and its corresponding edges are highlighted while the other properties are made transparent. Edges connecting the selected node and target nodes are colored according to the target nodes. For example, the arcs are blue colored when there are connections to the precuneus in the left hemisphere.

So only the connections which have more than 900 streamlines would be selected. The plot represents the number of streamlines along the preserved connections scaled down by a factor of 10 for ease of representation.

For interactive visualization, the cortical region caudal middle frontal in the left hemisphere is selected. It has prominent connections to the cortical regions superior frontal, rostra middle frontal and precuneus in the left hemisphere. Weak connection to the cortical region parsopercularis is also well represented by this diagram.

Overall, this comprehensive diagram is a systematic representation of whole brain connectivity. It can be used to analyze brain connections at the subject level or the group level.

## 4.3 Feature Analysis

Once the connectivity matrices were ready, it was important to investigate an effective connectivity metric and determine importance of within ROI connections. From the preprocessing pipeline presented in subsection 3.2.3 there were three types of connectivity metrics obtained for each subject. These were number of streamlines, the mean streamline length and the mean FA. Each of these features encodes a different biological property of ROI-to-ROI connections and gave different classification results. There is no current consensus on which feature qualifies as an effective measure of connectivity between any two nodes (Yeh et al., 2020). The number of streamlines was selected to be the major focus of the classification tasks due its superiority in classification performance, which will be illustrated subsequently. Further, exclusion of self loops from the connectivity matrices will be experimentally justified.

### 4.3.1 Differences in connectivity metric

As mentioned above, it was important to explore different types of connectivity metrics obtained from the connectivity matrices constructed using the methodology illustrated in Fig. 3.1b. Considering the z-score distributions of ROI connections separately for males and females was taken as a method for data evaluation. A histogram for the three different feature or connectivity types could help speculate how well they could separate between the two classes.

The histograms were formed using data (containing both data samples from males and females) in the training set. Each feature was then standardized by removing the mean and scaling it to unit variance. After scaling the feature value for each subject is represented by a z statistic. The mean of the z statistic (of one

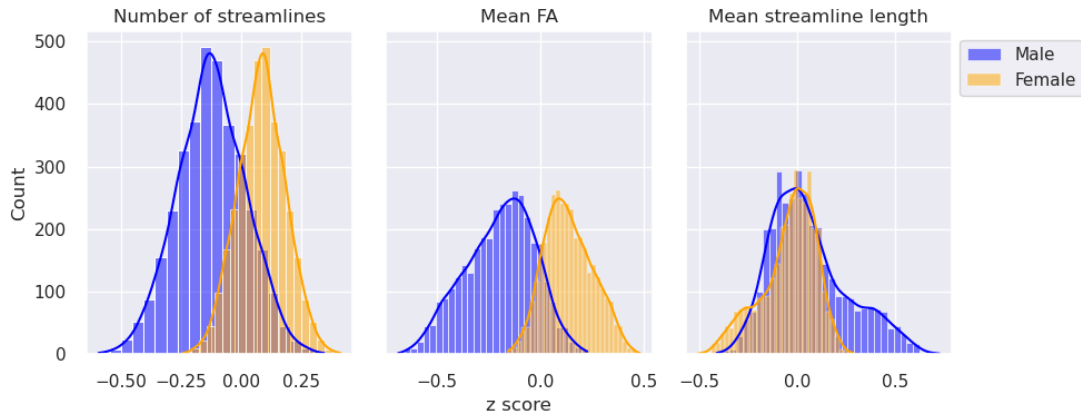


**Figure 4.3:** Three overlaid histograms representing the frequency of mean z-scores for different types of features. The orange histograms are for females and blue ones are for males. The y-axis represents the number of between ROI connections.

feature) is zero for all training subjects. However, the differences are prevalent when separate means are taken for the two genders. For each connection, there was one z-score for males and another for females depending on the connectivity metric. For each connectivity metric there are 3486 features which help form the distribution represented in Fig. 4.3.

From the distributions, it is evident that the number of streamlines is a good metric for gender classification. It's histogram is shows a smooth Gaussian distribution for males and females, and has significantly higher peaks than those for the other two features. Even though the mean FA features have a smaller overlap visually, the variance of these histograms is high.

From the differences in z-score distribution, it can be inferred that women on an average have more number of streamlines as compared men, for the same connections. This observation is coherent with evidence in Szalkai et al., 2015 showing that women have more densely connected brains than men. Further, women have higher white matter to grey matter ratio and hence the number of streamlines detected for women is higher (Taki et al., 2011).

The mean FA plots illustrate that women have higher mean FA values than men. Conversely, an opposite trend is seen in the case of mean streamline length. Women have lower z-scores, which points that shorter streamline lengths. Currently, there are no conclusive results for benchmarking such a distribution as gender differences prevail depending on ROIs being considered (Kanaan et al., 2012). For the mean FA, it is difficult to conclude that female brains have higher FA values since existing studies in whole brain connectivity do not provide conclusive results (Ingalhalikar et al., 2014). The shorter streamline lengths in women seem plausible, on average

Label	Metric	Feature	T statstic	P value
Personality Traits	Balanced accuracy	Mean FA	-0.196	0.846
		Mean streamline length	0.156	0.876
		Number of streamlines	-1.248	0.217
	Area under ROC curve	Mean FA	0.071	0.944
		Mean streamline length	1.332	0.188
		Number of streamlines	-1.42	0.161
Gender	Balanced accuracy	Mean FA	0.396	0.695
		Mean streamline length	2.068	0.048
		Number of streamlines	0.98	0.335
	Area under ROC curve	Mean FA	0.491	0.627
		Mean streamline length	3.875	0.001
		Number of streamlines	2.199	0.036

**Table 4.1:** Results for a paired samples t-test on the test set. The paired samples are the classification metrics of the data with and without the inclusion of self loops. The p values correspond to t-test of two arrays for the same classification metric constructed using methodology in subsection 3.3.2.

women's brains are smaller than that of men (Ankney, 1992).

The results for the number of streamlines and the mean streamline length are coherent with *a priori* knowledge and evidence in literature. These features could have contained biases as the tractography was carried out in individual subject's space. Such biases were corrected for comparing the streamline count or length for different subjects using informed filtering from the SIFT algorithm (Yeh et al., 2020).

The experiments stated above help establish the effectiveness of streamline count as a connectivity metric. It can discriminate well between gender and gives a biologically coherent measure of brain connectivity.

### 4.3.2 Self loops

Evaluation of the importance of self loops was carried out on the basis of the experiment mentioned in subsection 3.3.2. The results in Table 4.1 were obtained by training the baseline experiments with and without the exclusion of self loops. The report values correspond to classification performance on the test data. A positive t-statistic in this case indicates that the classification performance is greater with the inclusion of self loops. Meanwhile, a negative t-statistic indicates the opposite

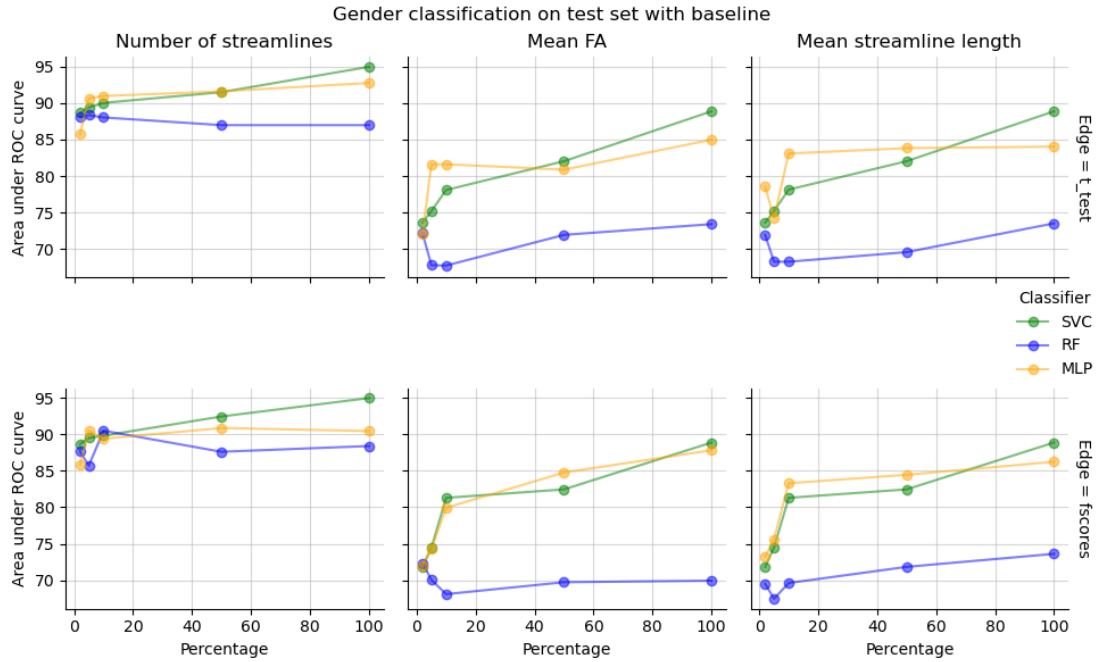


**Figure 4.4:** Baseline analysis for gender classification. The AUC represented as a function of percentage of features.

trend. Statistical inference on this data indicates that the exclusion of self loops from the data analysis does not have a statistically significant effect on classification accuracy. The statistics obtained from the analysis of both the target labels, i.e. the personality traits and gender labels do not lie in a significant confidence interval. The p-values in Table 4.1 are indicative of these results with most of them  $p > 0.05$ .

Consider the statistics for the mean FA feature. All the p-values are  $p > 0.05$  and the t-statistic has opposite signs when it comes to considering two cases for personality classification. The first being balanced accuracy and the second as the AUC. The t-statistic for the first case is  $t = -0.196$  and for the second case is  $t = 0.071$ . This opposite trend for two different measures is indicative of the fact that there is no general trend of classification performance.

With this investigation it became clear that the self loops can be eliminated from the data of all subjects. This ensured that the MEWS solver based technique as well as the baseline filters features from the same set of raw data.

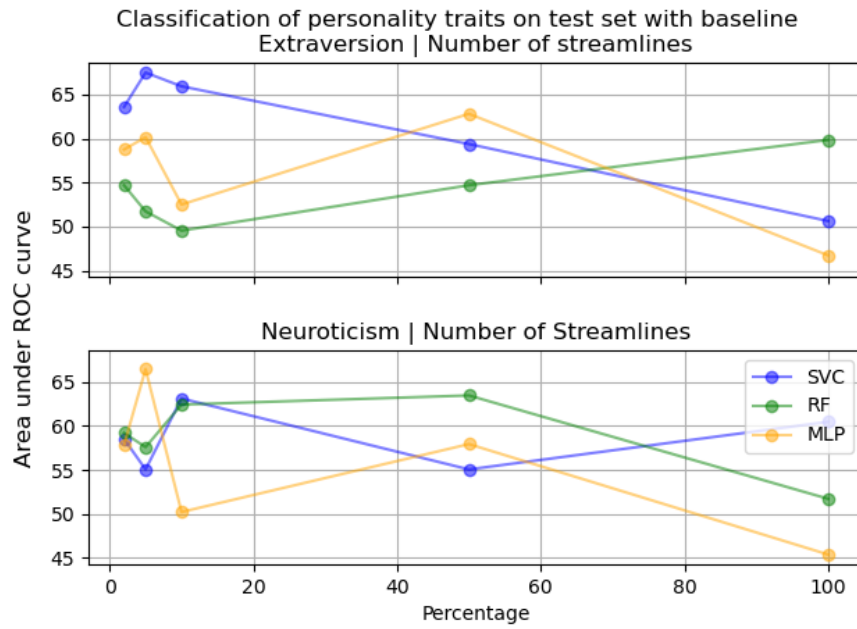


**Figure 4.5:** Baseline analysis on the basis of personality traits using pearson correlation coefficient as a filter method. For neuroticism, there is a trend of increase in performance with only a subset of original features using all three classifiers. The trend for the MLP shows greater than 65% AUC for top 5% of features while 45% without any feature selection. Classification performance on extraversion label increases with decrease in the number of features for classification with MLP and SVC. The strongest trend seen with the SVC, the AUC increases from 50% (without feature selection) to around 67% (using top 5% of the original features). The overall trend for neuroticism and extraversion illustrates that it is useful to do some feature selection in order to predict these traits.

## 4.4 Baseline analysis

The baseline analysis mentioned in subsection 3.4.1 with the parameter  $k \in \{2, 5, 10, 50, 100\}$  was chosen to select the best performing connectivity metric. Here,  $k$  denotes the percentage of features to be preserved. One important research question to be explored with this analysis was to determine whether doing any feature selection gives an added advantage to the classification accuracy.

From Fig. 4.4, it became evident that the number of streamlines served as a good metric for gender classification. There was only a loss of around 5% performance for AUC while reducing the percentage of features from 100% to 5% for both types of edge representations, i.e. the t-test and f-scores and all three classifiers. In terms of number of features this meant that even choosing 175 out of 3486 features, most of the discriminative information could be preserved.

The baseline analysis of the different personality traits was more complex as compared to gender classification. All the possibilities of connectivity metrics and five different personality traits were considered in the pipeline. However, an overall trend could be observed only with neuroticism and extraversion. For these two personality traits, feature selection lead to much improved classifier performance with all three classifiers. A steep increase can be seen for extraversion where the AUC increases from about 50% (random chance) to about 68%.

For both the personality traits and the gender based classification, feature selection is profitable. In case of gender classification, an interpretability-performance trade-off was observed. This trade-off is between the increase in interpretability with the decrease in the number of preserved features and decrease in classifier performance with the decline in the number of features. For personality classification the feature selection leads to a clear increase in interpretability and performance.

## 4.5 Tracing back to original features

A major motivation behind implementing the MEWS based technique for this thesis was interpretability of the feature selection. In this section the interpretability of the set of features selected by the baseline as well as the solver based implementation are compared. It is observed that the solver based method is superior to the traditional baseline method due to connectedness of the output features.

The two subsequent subsections present visualizations for the features selected by both the feature selection techniques. Furthermore, the subsection 4.5.1 provides an insight into how the solver implementation preserves edges.

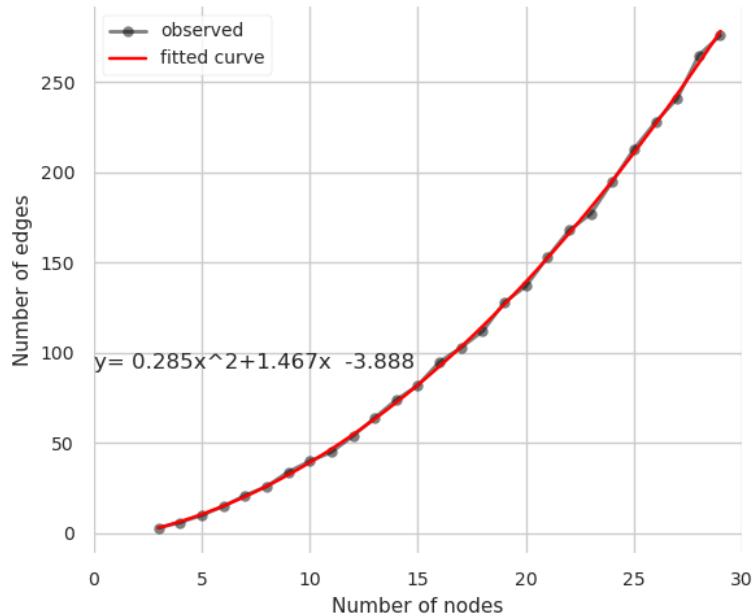


**Figure 4.6:** The number of edges preserved by the MEWS solver as a function of the number of nodes supplied to the parameter  $m$  (Eq. 3.3). The black dots illustrate the number of edges preserved for inputs  $m \in [4, 30]$ . A quadratic curve was fitted to map this trend. The red line represents the fitted model with the parameters mentioned in the figure. Using the fitted polynomial the number of edges preserved could be predicted before running the solver. This saved computational time and effort since the nature of output graphs could be predicted beforehand.

### 4.5.1 Solver features

For classification with the solver based technique detailed in section 2.5, the number of nodes preserved could be specified using a parameter  $m$ . Determining the order of growth in the number of edges as a function of  $m$  was important to trace back the MEWS selected features to the original dataframe. Figure 4.6 shows a quadratic form with the number of edges  $y$  as a function of the number of nodes  $x$ . This behavior is expected as the graph is supposed to be connected; i.e. there exists an edge between any two nodes in the graph. Using these results, the extent of interpretability from the solver results could be controlled.

### 4.5.2 Baseline Solver comparison

In order to compare the two feature selection techniques, a separate input graph had to be created for a two use cases according to Figure 3.3. These two use cases

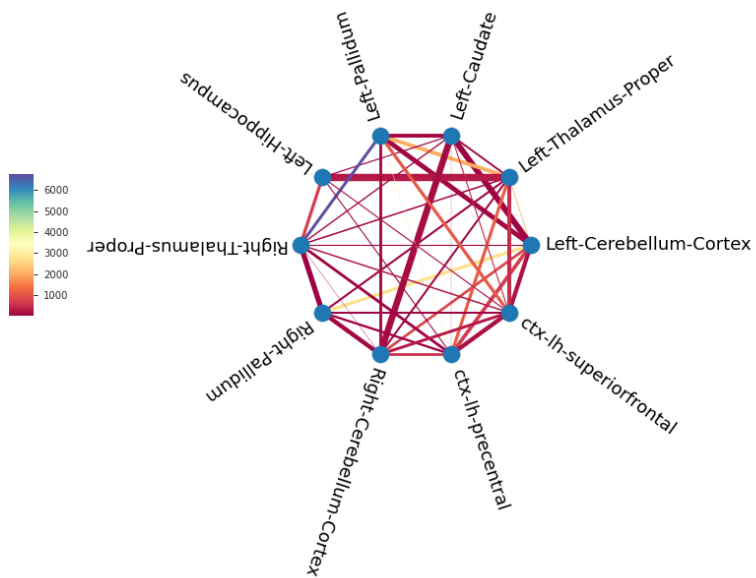


**Figure 4.7:** 10 most important nodes out of 84 determined using the MEWS solver for gender classification. The edge widths represent the f-scores of and color represents the number of streamlines between the two regions. A higher number of streamlines does not directly correspond to a higher fscore. 6 of the 10 selected nodes are subcortical regions; the thalai, the pallidai, the left hippocampus and left caudate while the remaining are cortical regions. This figure depicts that gender differences might be more prominent in subcortical brain networks than cortical brain networks.

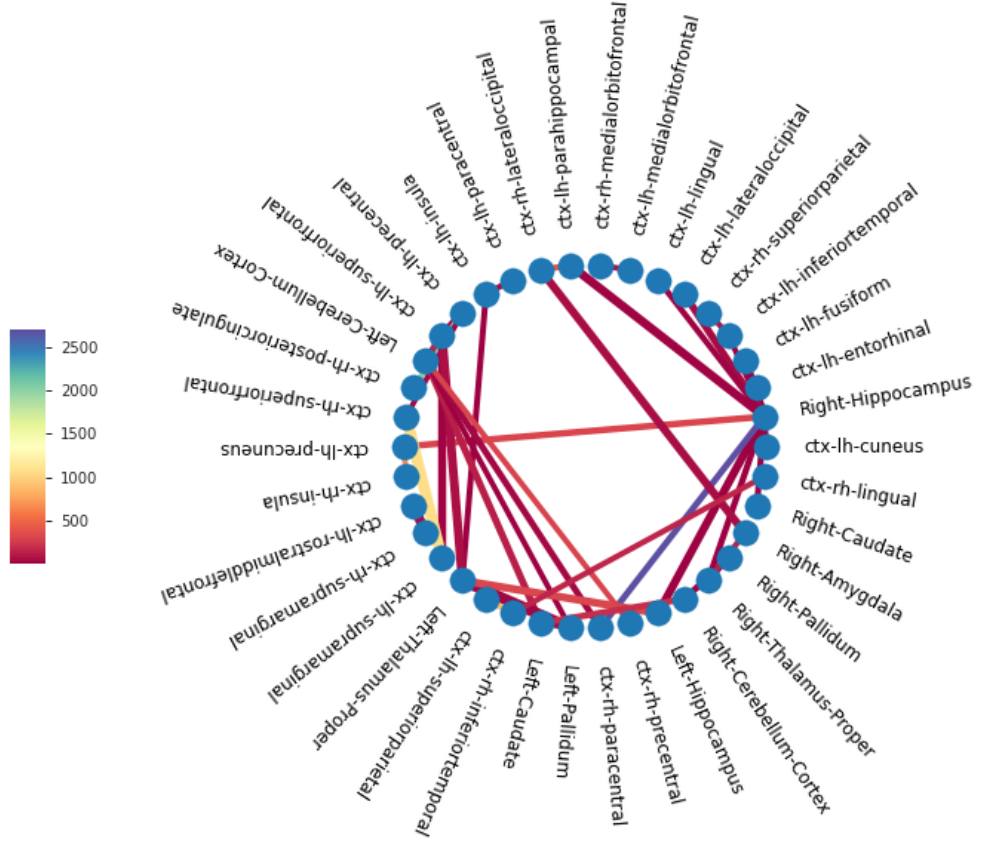


**Figure 4.8:** 41 most important features, and consequently 38 nodes preserved using baseline analysis for gender classification. The edge widths represent the f-scores and color represents the number of streamlines between the two regions. This figure shows that the baseline analysis does take graph topology into account and the features selected by this technique are not informative about any patterns such as the ones inferred using MEWS solver in Fig. 4.7.

were visualized to compare the interpretability of predictions from the solver and baseline analysis.

In the first use case, the type of feature is number of streamlines, the target label is gender, edge representation is f-score and feature selection is solver with 10 nodes preserved in the subgraph. In the second use case, all the parameters were the same as the first use case except for baseline as the feature selection technique and number of edges as 41 for comparison with 41 edges preserved in the first use case (using polynomial in Fig. 4.6). The visualizations of these two use cases are Fig. 4.7 and Fig. 4.8. In both the visualizations, the edge widths represent the f-scores and the color represents the group averaged number of streamlines. The group averaged number of streamlines and f-scores are determined on the training data only.

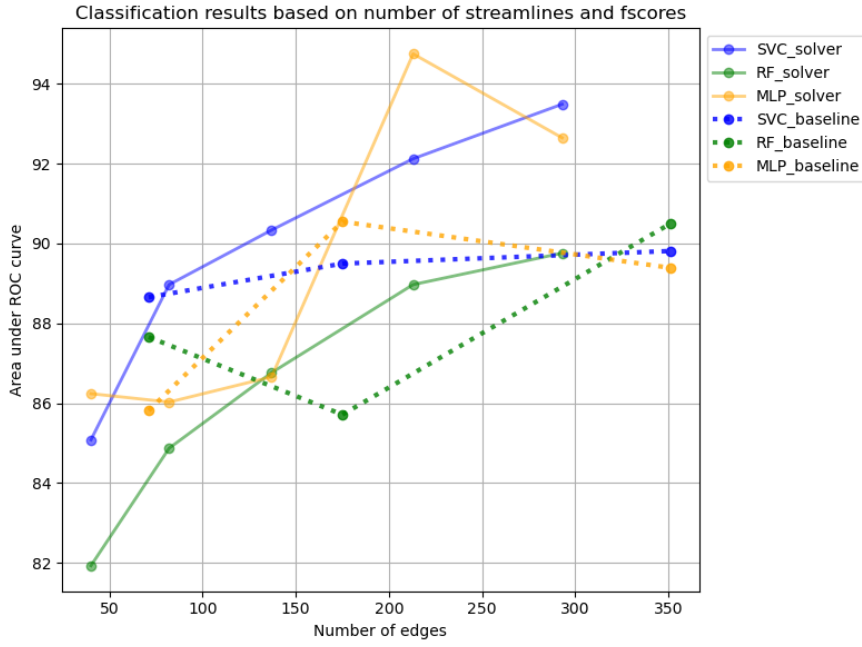
In Fig. 4.7 the MEWS solver based implementation reduces the input graph and preserves 10 nodes along with 41 edges. It can be seen that the graph is well connected and structured. 6 out of 10 most important nodes are subcortical regions. These regions are the thalai, the pallidai, the left hippocampus and left caudate. The lookup table from the Desikan-Killiany Atlas had total 70 nodes for cortical regions and 14 nodes for subcortical ones, the ratio of selected nodes for subcortical regions 0.43 is higher than for cortical regions 0.06. Such a pattern indicates that gender differences might be more prominent in networks of subcortical regions rather than cortical ones. Figure 4.8 exemplifies the fact that the baseline method selects the same number of edges (41) by preserving 38 nodes, almost four times the nodes preserved by the solver. The graph is not connected and contains isolated edges, very often nodes with a degree of only 1.

Figure 4.7 and Fig. 4.8 illustrate the superiority of the MEWS solver generated subgraphs over baseline features in terms of interpretability. In a research setting, the MEWS solver method would hence be more beneficial since it provides more interpretable results. With this technique it becomes easier to determine the subnetworks related to a particular target variable.

## 4.6 Model performance

Classification performance on the target label varied depending on the parameters of the data given to the classifier according to Figure 3.3. This section will present the classification results for solver and personality traits respectively.

For the classification of gender, the comparison of classification performance was easily interpretable. At first, the baseline experiments for  $k \in \{2, 5, 10\}$  were compared with solver nodes  $m \in \{5, 10, 15, 25, 30\}$  due to computational complexity



**Figure 4.9:** Comparison of AUC for gender classification on the independent test set. The performance of three classifiers SVC, RF and MLP on the basis of features filtered according to the solver and baseline experiments respectively.

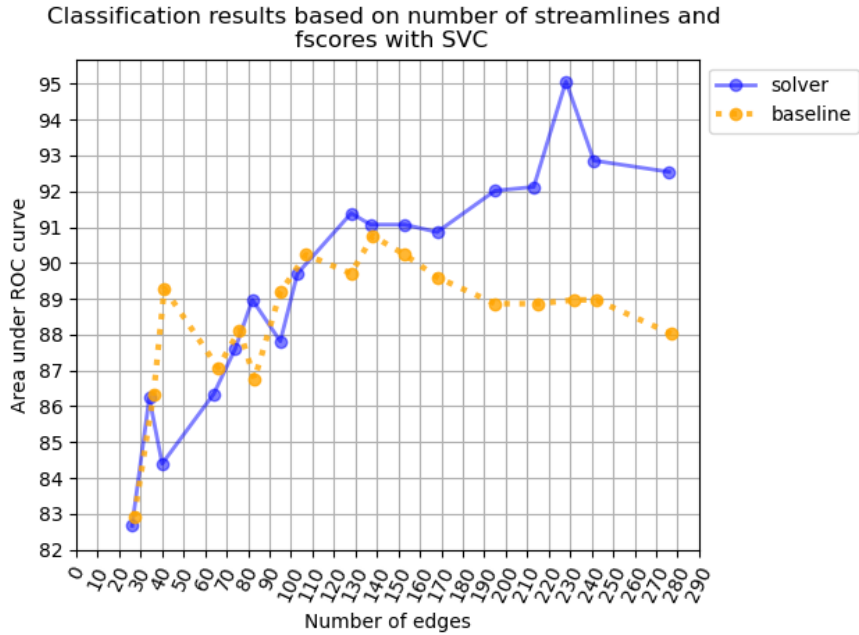


**Figure 4.10:** Gender classification using solver and baseline for the exact same number of features selected in each case.

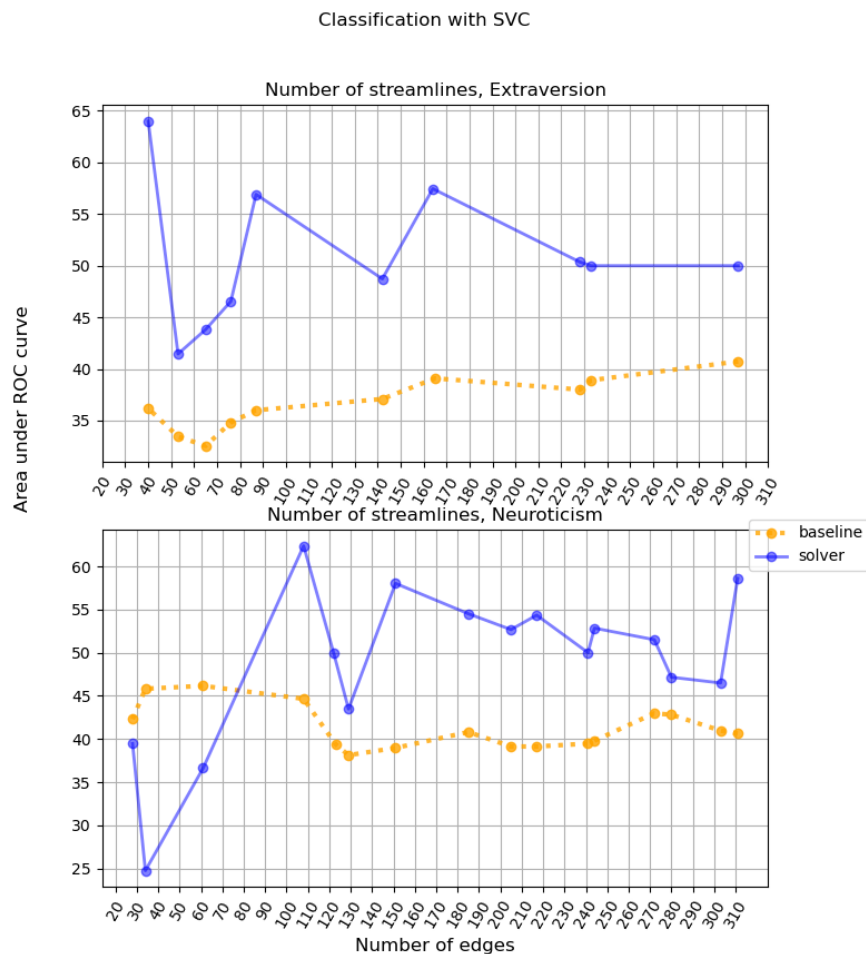


**Figure 4.11:** Comparison of solver and baseline for classification of personality traits.

of the exhaustive search. Figure 4.9 was used to determine the which classifier performs the best and gives results free from overfitting.

The SVM based classification produced the most stable results out of the three classifiers used and was taken as the choice for an exhaustive search. Once the classifier was decided upon, classification performance for a higher number of data points were sampled. This time the parameter top  $k$  percentile of features to be preserved with the baseline was decided by using the polynomial in Fig. 4.6 so that the number of edges are comparable between the solver and the baseline.

The subsequent results using SVC (Fig. 4.10) clearly indicate a cutoff number of edges, i.e. precisely 137 (obtained from the function in Fig. 4.6). The MEWS solver definitely does better than the baseline analysis in terms of classification performance after the cutoff value of 137 edges. Even for the number of edges below 137, the results remain comparable. It can be inferred that using the MEWS solver, after 137 edges or 20 nodes (using Fig. 4.6) the solver offers more interpretability as well as better classification performance than the baseline. Preserving less than 20 nodes leads to a reduction in classifier performance but an increase in ease of visualization and interpretability. With  $m > 20$  nodes, there is a decrease in interpretability but an increase in classifier performance.

For classification of personality traits using SVC, the results are not much higher than a random chance. However, the MEWS method performed much better than baseline analysis throughout the range of feature numbers presented in Fig. 4.11. For the classification of neuroticism the solver is able to achieve a maximum AUC of around 64% which is a better than the maximum score of 40% by a margin of 24%. Similarly, for neuroticism the SVC achieves about 62% accuracy with the MEWS solver and a little over 45% for the baseline.

On the basis of the classification results for personality traits and gender, it can be concluded that the MEWS solver is a better feature selection technique than the baseline analysis.

### 4.6.1 Best parameters

In this section, the parameters of the best estimators for gender classification will be presented. The SVC gave most stable results as compared to other classifiers. The best performing estimators are determined using Fig. 4.10. For gender classification using the solver, the maximum AUC of 95% for the independent test set could be achieved. This performance is obtained for 237 edges corresponding to 26 nodes. Using the baseline technique, the best estimator could achieve 91% area under curve for around 138 edges.

In Table 4.2 the parameters of the best estimators for the MEWS solver based

method and baseline used for gender classification using number of streamlines and f-scores will be presented.

Hyperparameter	Solver	baseline
C	5.9	0.522
Gamma	4e-4	8e-4
kernel	rbf	rbf
class weight	balanced	None

**Table 4.2:** Cross validation parameters for SVC trained for gender classification. The parameters which give the best area under the curve for the use case mentioned in the section above have been presented



# 5 Discussion

In this work classification on the basis of a subgraph derived from structural brain connectivity was the major challenge. According to Figure 3.3, a large combination of possibilities for designing the classification task was tried in order to obtain the most interpretable and statistically significant results. The goal was to not only gain the maximum classification performance but also to make a generalized framework in which each step can be visualized. The architecture remains specific to structural brain connectivity but is generalizable enough to predict different target variables. Major considerations for the task design such as connectivity features and graph structure are presented in the subsequent sections.

## 5.1 Connectivity features

There were three types of features used as representatives of structural brain connectivity. The number of streamlines, the mean FA of streamlines and the mean streamline length. Generally, the number of streamlines seemed to have performed much better than the other two features considering the AUC for classification of gender on an independent test set. It performed better with both baseline and solver based methods, regardless of the labels i.e. personality trait or gender. The superior performance of the number of streamlines using the MEWS solver based approach seems plausible due to the incorporation of a particular constraint in the pipeline. This constraint was that a feature in the connectome is included in the input graph for the solver if and only if there is at least one streamline present for all subject. Such a condition remained unique to the number of streamlines. Perhaps trying such conceptual *a priori* knowledge with the mean FA and mean streamline length could yield different results.

Furthermore, streamline quantification bias in the analysis pipeline was corrected with the help of informed fiber filtering. This made the number of streamlines an effective measure of connectivity. There is currently no ground truth regarding which of these three connectivity measures is the best to formulate the relationship between any two ROIs. The mean FA could also provide a biologically accurate meaning of connectivity considering it is independent of size of a person's

brain unlike the mean streamline length. The mean streamline length could not have performed well because it might be sensitive to the differences in the sizes of subject's brains. The brain size could then become a confounding factor where higher streamline lengths are an artefact of bigger brain size.

## 5.2 Filter method

Different types of statistical coefficients could be used as filters for scoring the raw features. Supervised filter methods were used instead of unsupervised filter methods since discriminative subnetworks relevant to a given target label were to be obtained. The f-score and p-value of the t-test were chosen for categorical variables and pearson correlation coefficient was used for continuous variables as their usage is standard in most neuroimaging studies.

The pearson correlation coefficient worked better than f-scores and t-test as a filter method for the personality traits. This was because it considers the linear nature of the personality trait coefficients. It performed well for the baseline experiments as well as the solver based feature selection. For both the cases the absolute value of the pearson correlation coefficient was taken because only the correlation was important, whether it is positive or negative correlation was not a matter of concern for the analysis. The pearson correlations could be easily thresholded by using a user defined threshold and opened the possibility for more experimentation. The f-score and the t-test were based on the binarization of the target variables according to the median values of the personality trait from the training set, this might lead to information loss and hence their lower numerical values.

For gender, which is categorical by definition, the t-test and the f-scores proved to be a good scoring technique. There was not any information loss considering these two statistics measure similar attributes of a particular feature: they measure how well a particular feature separates the two classes. This type of selection worked quite well with gender variables for both baseline and solver analysis.

## 5.3 Node weights

Different types of node weightings were tried to form the subgraph apart from a constant value of  $-0.01$  assigned to all nodes presented in the results. It was required to eliminate nodes from the original input graph and preserve at most  $m$  nodes specified. Since all the edge weights were positive, the negative weights of the nodes ensured that the overall positive effect of the edge weights overcame the

cost of keeping an extra node.

Assigning the nodes a constant weight of zero resulted in all nodes getting preserved. This happened since there were no negative edges so none of the edges get eliminated. The sum of all original edge weights remains the highest according to Eq. (2.19). This effect was observed since the preprocessing step of the implementation in Loboda et al., 2016 was disabled and all nodes in the input graph remained well connected. Similarly, assigning any type of positive node weight was incompatible for the implementation in subsection 3.4.2 since no nodes and edges would get eliminated.

## 5.4 Constraining number of nodes

As mentioned in previous sections. The MEWS solver implementation was give a constraint to preserve a specified number of nodes in order to indirectly control the number of edges preserved. Without this constraints, the results produced by the solver were impractical for comparison with the baseline.

Consider an example, the input graph was formed by using the number of streamlines as the raw feature, the f-scores for gender classification as the edge representation. The output graph from the solver had an arbitrary number of edges and this result remained the same each time. This gave only two instances of comparison with the baseline. The first using the input graph containing all the edges and the second for the number of edges preserved in the output graph. With only two data points, a general trend of classification performance could not be clearly determined.

When the parameter  $m$  for specifying the number of nodes was added. For each input graph different output graphs could be generated on the basis of the number of nodes preserved. All these graphs contained a different number of edges which could be matched to the  $k$  percentile of features preserved by the baseline. Hence, the incorporation of the constraint on the number of nodes was pivotal to evaluate the performance of the features selected by the MEWS solver.

## 5.5 Personality classification

The classification of personality traits was a methodologically challenging task. The personality traits are continuous in nature. A regression task was not formulated for these continuous variables since the regression task would be incompatible with the pipeline. The major focus of this thesis was to formulate a discriminative subgraph.

Binning the continuous personality traits them for a classification task definitely lead to information loss. However, this information loss was incorporated in the classification technique by determining the pearson correlation coefficient of the personality traits with the feature. The evidence of information loss was also observed by trying to give the input graphs based on t-test and f-scores to the solver for classification of personality traits. However, t-test coefficients and the f-score coefficients had low standard deviations which made account for the fact that they could not be able to well distinguish between different feature relations to personality traits.

# 6 Conclusion

Analyzing the properties of structural brain networks is a challenging task. Especially classification based on dense graphs derived from brain connectivity requires a well assessed scientific methodology. The pipeline implemented in this work is tailored towards accurate classification from structural brain connectivity. Three major characteristics of the pipeline make it apt for usage in clinical as well as behavioral research. These aspects are the consideration of graph topology, visualization at each step and a generalized approach.

First, the graph topology incorporated using the MEWS technique provides interpretable and visualizable results. This framework enables effective classifier training and statistical analysis. The structure of the output subgraph can be controlled with the number of nodes to be preserved, the type of ranking or the type of connectivity measure to use. Especially, the preservation of a specified number of nodes can be used to rank node importance additional to feature importance. The number of edges can also be controlled indirectly with the number of nodes. This makes it a better alternative to the state of the art filter based methods used in neuroimaging studies.

Second, all the steps right from the preprocessing of the connectome to the features selected for model training had a visual analog. Detailed visualizations that help evaluate biological correspondence of the data preparation and selection have been incorporated into the pipeline. These types of visualization can help evaluate significant biases or errors that play a role in making an *in-silico* model of brain connectivity.

Third, the pipeline can be implemented for any type of target variable. Be it a categorical or binary variable such as gender or a continuous variable such as a personality trait. One important factor is that special consideration was given to remove the effects of information loss for categorical variables. Linear coefficient was used to account for the linear relationship between a particular feature and the continuous variable. For a binary variable group based differences were evaluated by grouping subjects. In this way information supervised filter methods were combined with graph topology considerations.

Overall, the method is novel but is not comprehensive on addressing all the challenges that come in the way of modeling structural brain connectivity. It

gives a controllable trade-off between model performance and interpretability. The pipeline could further be improved by encoding more *a priori* knowledge from neurobiology and consideration of a larger dataset and using different imaging modalities. Another important observation could be to see if the features selected by the diffusion matrices correspond to the features selection by using functional connectivity matrices formed using fMRI data.

# References

- [1] E. Althaus, M. Blumenstock, A. Disterhoft, A. Hildebrandt, and M. Krupp. “Algorithms for the Maximum Weight Connected k-Induced Subgraph Problem”. In: *International Conference on Combinatorial Optimization and Applications*. Springer. 2014, pp. 268–282 (cit. on p. 20).
- [2] C. D. Ankney. “Sex differences in relative brain size: The mismeasure of woman, too?” In: *Intelligence* 16.3-4 (1992), pp. 329–336 (cit. on p. 48).
- [3] D. S. Bassett and O. Sporns. “Network neuroscience”. In: *Nature neuroscience* 20.3 (2017), pp. 353–364 (cit. on p. 17).
- [4] T. E. Behrens, H. Johansen-Berg, M. Woolrich, S. Smith, C. Wheeler-Kingshott, P. Boulby, G. Barker, E. Sillery, K. Sheehan, O. Ciccarelli, et al. “Non-invasive mapping of connections between human thalamus and cortex using diffusion imaging”. In: *Nature neuroscience* 6.7 (2003), pp. 750–757 (cit. on p. 16).
- [5] Y. Bengio and O. Delalleau. “On the Expressive Power of Deep Architectures”. In: *Algorithmic Learning Theory*. Ed. by J. Kivinen, C. Szepesvári, E. Ukkonen, and T. Zeugmann. Berlin, Heidelberg: Springer Berlin Heidelberg, 2011, pp. 18–36. ISBN: 978-3-642-24412-4 (cit. on p. 26).
- [6] F. Bloch. “Nuclear Induction”. In: *Phys. Rev.* 70 (7-8 Oct. 1946), pp. 460–474. DOI: 10.1103/PhysRev.70.460. URL: <https://link.aps.org/doi/10.1103/PhysRev.70.460> (cit. on p. 6).
- [7] F. Bloch. “Nuclear induction”. In: *Physical review* 70.7-8 (1946), p. 460 (cit. on p. 11).
- [8] D. Brogioli and A. Vailati. “Diffusive mass transfer by nonequilibrium fluctuations:Fick’s law revisited”. In: *Physical Review E* 63.1 (Dec. 2000). ISSN: 1095-3787. DOI: 10.1103/physreve.63.012105. URL: <http://dx.doi.org/10.1103/PhysRevE.63.012105> (cit. on p. 9).
- [9] C. Burges and C. J. Burges. “A Tutorial on Support Vector Machines for Pattern Recognition”. In: *Data Mining and Knowledge Discovery* 2 (Jan. 1998), pp. 121–167. URL: <https://www.microsoft.com/en-us/research/publication/a-tutorial-on-support-vector-machines-for-pattern-recognition/> (cit. on p. 23).

- [10] K. A. Clark, K. H. Nuechterlein, R. F. Asarnow, L. S. Hamilton, O. R. Phillips, N. S. Hageman, R. P. Woods, J. R. Alger, A. W. Toga, and K. L. Narr. “Mean diffusivity and fractional anisotropy as indicators of disease and genetic liability to schizophrenia”. In: *Journal of psychiatric research* 45.7 (2011), pp. 980–988 (cit. on p. 12).
- [11] B. A. Cociu, S. Das, L. Billeci, W. Jamal, K. Maharatna, S. Calderoni, A. Narzisi, and F. Muratori. “Multimodal functional and structural brain connectivity analysis in autism: A preliminary integrated approach with EEG, fMRI, and DTI”. In: *IEEE Transactions on Cognitive and Developmental Systems* 10.2 (2017), pp. 213–226 (cit. on p. 2).
- [12] D. Colquhoun. “The reproducibility of research and the misinterpretation of p-values”. In: *Royal society open science* 4.12 (2017), p. 171085 (cit. on p. 19).
- [13] S. Cook, T. Jarrell, C. Brittin, Y. Wang, A. Bloniarz, M. Yakovlev, K. Nguyen, L. Tang, E. Bayer, J. Duerr, H. Bülow, O. Hobert, D. Hall, and S. Emmons. “Whole-animal connectomes of both *Caenorhabditis elegans* sexes”. In: *Nature* 571 (July 2019), p. 63. DOI: 10.1038/s41586-019-1352-7 (cit. on p. 17).
- [14] P. T. Costa Jr and R. R. McCrae. “The five-factor model of personality and its relevance to personality disorders”. In: *Journal of personality disorders* 6.4 (1992), pp. 343–359 (cit. on p. 32).
- [15] F. Dell’Acqua and J.-D. Tournier. “Modelling white matter with spherical deconvolution: How and why?” In: *NMR in Biomedicine* 32.4 (2019), e3945 (cit. on p. 14).
- [16] M. Descoteaux, R. Deriche, T. R. Knosche, and A. Anwander. “Deterministic and probabilistic tractography based on complex fibre orientation distributions”. In: *IEEE transactions on medical imaging* 28.2 (2008), pp. 269–286 (cit. on p. 15).
- [17] R. S. Desikan, F. Ségonne, B. Fischl, B. T. Quinn, B. C. Dickerson, D. Blacker, R. L. Buckner, A. M. Dale, R. P. Maguire, B. T. Hyman, et al. “An automated labeling system for subdividing the human cerebral cortex on MRI scans into gyral based regions of interest”. In: *Neuroimage* 31.3 (2006), pp. 968–980 (cit. on p. 31).
- [18] O. Dietrich, A. Biffar, A. Baur-Melnyk, and M. Reiser. “Technical aspects of MR diffusion imaging of the body”. In: *European Journal of Radiology* 76 (Mar. 2010), pp. 314–22. DOI: 10.1016/j.ejrad.2010.02.018 (cit. on p. 10).
- [19] A. Fornito, A. Zalesky, and M. Breakspear. “The connectomics of brain disorders”. In: *Nature Reviews Neuroscience* 16.3 (2015), pp. 159–172 (cit. on p. 17).

- [20] S. Gerhard, A. Daducci, A. Lemkaddem, R. Meuli, J.-P. Thiran, and P. Hagmann. “The connectome viewer toolkit: an open source framework to manage, analyze, and visualize connectomes”. In: *Frontiers in neuroinformatics* 5 (2011), p. 3 (cit. on p. 33).
- [21] A. Ghosh and R. Deriche. “A survey of current trends in diffusion MRI for structural brain connectivity”. In: *Journal of neural engineering* 13.1 (2015), p. 011001 (cit. on p. 9).
- [22] M. F. Glasser, S. N. Sotiropoulos, J. A. Wilson, T. S. Coalson, B. Fischl, J. L. Andersson, J. Xu, S. Jbabdi, M. Webster, J. R. Polimeni, D. C. Van Essen, and M. Jenkinson. “The minimal preprocessing pipelines for the Human Connectome Project”. In: *NeuroImage* 80 (2013). Mapping the Connectome, pp. 105–124. ISSN: 1053-8119. DOI: <https://doi.org/10.1016/j.neuroimage.2013.04.127>. URL: <http://www.sciencedirect.com/science/article/pii/S1053811913005053> (cit. on pp. 29, 33).
- [23] A. Hagberg, P. Swart, and D. S Chult. *Exploring network structure, dynamics, and function using NetworkX*. Tech. rep. Los Alamos National Lab.(LANL), Los Alamos, NM (United States), 2008 (cit. on p. 41).
- [24] M. Haouari, N. Maculan, and M. Mrad. “Enhanced compact models for the connected subgraph problem and for the shortest path problem in digraphs with negative cycles”. In: *Computers & operations research* 40.10 (2013), pp. 2485–2492 (cit. on p. 22).
- [25] T. Hastie, R. Tibshirani, and J. Friedman. *The elements of statistical learning: data mining, inference, and prediction*. Springer Science & Business Media, 2009 (cit. on p. 24).
- [26] HCP. “WU-Minn HCP 900 Subjects Data Release: Reference Manual”. In: (2015) (cit. on p. 29).
- [27] M. K. Hobert, V. M. Stein, P. Dziallas, D. C. Ludwig, and A. Tipold. “Evaluation of normal appearing spinal cord by diffusion tensor imaging, fiber tracking, fractional anisotropy, and apparent diffusion coefficient measurement in 13 dogs”. In: *Acta Veterinaria Scandinavica* 55.1 (2013), p. 36 (cit. on p. 43).
- [28] M. Ingallalikar, A. Smith, D. Parker, T. D. Satterthwaite, M. A. Elliott, K. Ruparel, H. Hakonarson, R. E. Gur, R. C. Gur, and R. Verma. “Sex differences in the structural connectome of the human brain”. In: *Proceedings of the National Academy of Sciences* 111.2 (2014), pp. 823–828 (cit. on p. 47).
- [29] I. Inza, P. Larrañaga, R. Blanco, and A. J. Cerrolaza. “Filter versus wrapper gene selection approaches in DNA microarray domains”. In: *Artificial intelligence in medicine* 31.2 (2004), pp. 91–103 (cit. on p. 19).

- [30] B. Jeurissen, J.-D. Tournier, T. Dhollander, A. Connelly, and J. Sijbers. “Multi-tissue constrained spherical deconvolution for improved analysis of multi-shell diffusion MRI data”. In: *NeuroImage* 103 (2014), pp. 411–426. ISSN: 1053-8119. DOI: <https://doi.org/10.1016/j.neuroimage.2014.07.061>. URL: <http://www.sciencedirect.com/science/article/pii/S1053811914006442> (cit. on p. 14).
- [31] B. Jeurissen, J.-D. Tournier, T. Dhollander, A. Connelly, and J. Sijbers. “Multi-tissue constrained spherical deconvolution for improved analysis of multi-shell diffusion MRI data”. In: *NeuroImage* 103 (2014), pp. 411–426 (cit. on p. 35).
- [32] D. Jones. *Diffusion MRI*. Oxford University Press, 2010. ISBN: 9780199708703. URL: <https://books.google.de/books?id=dbZCMMePD52AC> (cit. on p. 12).
- [33] R. A. Kanaan, M. Allin, M. Picchioni, G. J. Barker, E. Daly, S. S. Shergill, J. Woolley, and P. K. McGuire. “Gender differences in white matter microstructure”. In: *PloS one* 7.6 (2012), e38272 (cit. on p. 47).
- [34] A. A. Loboda, M. N. Artyomov, and A. A. Sergushichev. “Solving generalized maximum-weight connected subgraph problem for network enrichment analysis”. In: *CoRR* abs/1605.02168 (2016). arXiv: 1605.02168. URL: <http://arxiv.org/abs/1605.02168> (cit. on pp. 19, 20, 29, 38, 40, 41, 63).
- [35] S. Mastrogiacomo, W. Dou, J. A. Jansen, and X. F. Walboomers. “Magnetic Resonance Imaging of Hard Tissues and Hard Tissue Engineered Bio-substitutes”. In: *Molecular Imaging and Biology* 21.6 (Dec. 2019), pp. 1003–1019. ISSN: 1860-2002. DOI: 10.1007/s11307-019-01345-2. URL: <https://doi.org/10.1007/s11307-019-01345-2> (cit. on p. 5).
- [36] W. McKinney et al. “pandas: a foundational Python library for data analysis and statistics”. In: *Python for High Performance and Scientific Computing* 14.9 (2011) (cit. on p. 29).
- [37] D. W. McRobbie, E. A. Moore, M. J. Graves, and M. R. Prince. *MRI from Picture to Proton*. 2nd ed. Cambridge University Press, 2006. DOI: 10.1017/CBO9780511545405 (cit. on p. 3).
- [38] J. Muller, M. Alizadeh, F. B. Mohamed, J. Riley, J. J. Pearce, B. Trieu, T.-W. Liang, V. Romo, A. Sharan, and C. Wu. “Clinically applicable delineation of the pallidal sensorimotor region in patients with advanced Parkinson’s disease: study of probabilistic and deterministic tractography”. In: *Journal of neurosurgery* 131.5 (2018), pp. 1520–1531 (cit. on p. 15).
- [39] G. J. Parker, H. A. Haroon, and C. A. Wheeler-Kingshott. “A framework for a streamline-based probabilistic index of connectivity (PICo) using a structural interpretation of MRI diffusion measurements”. In: *Journal of Magnetic Resonance Imaging: An Official Journal of the International Society for Magnetic Resonance in Medicine* 18.2 (2003), pp. 242–254 (cit. on p. 34).

- [40] F. Pedregosa, G. Varoquaux, A. Gramfort, V. Michel, B. Thirion, O. Grisel, M. Blondel, P. Prettenhofer, R. Weiss, V. Dubourg, J. Vanderplas, A. Passos, D. Cournapeau, M. Brucher, M. Perrot, and E. Duchesnay. “Scikit-learn: Machine Learning in Python”. In: *Journal of Machine Learning Research* 12 (2011), pp. 2825–2830 (cit. on p. 29).
- [41] J. Ridgway. “Cardiovascular magnetic resonance physics for clinicians: Part I”. In: *Journal of cardiovascular magnetic resonance : official journal of the Society for Cardiovascular Magnetic Resonance* 12 (Nov. 2010), p. 71. DOI: 10.1186/1532-429X-12-71 (cit. on p. 8).
- [42] A. Romano, G. D’andrea, G. Minniti, L. Mastronardi, L. Ferrante, L. Fantozzi, and A. Bozzao. “Pre-surgical planning and MR-tractography utility in brain tumour resection”. In: *European radiology* 19.12 (2009), p. 2798 (cit. on p. 14).
- [43] R. Sala-Llonch, D. Bartrés-Faz, and C. Junqué. “Reorganization of brain networks in aging: a review of functional connectivity studies”. In: *Frontiers in psychology* 6 (2015), p. 663 (cit. on p. 1).
- [44] A. Sarica, A. Cerasa, and A. Quattrone. “Random Forest Algorithm for the Classification of Neuroimaging Data in Alzheimer’s Disease: A Systematic Review”. In: *Frontiers in Aging Neuroscience* 9 (2017), p. 329. ISSN: 1663-4365. DOI: 10.3389/fnagi.2017.00329. URL: <https://www.frontiersin.org/article/10.3389/fnagi.2017.00329> (cit. on p. 2).
- [45] S. Shi and F. Nathoo. “Feature Learning and Classification in Neuroimaging: Predicting Cognitive Impairment from Magnetic Resonance Imaging”. In: *2018 4th International Conference on Big Data and Information Analytics (BigDIA)*. IEEE. 2018, pp. 1–5 (cit. on p. 18).
- [46] A. Sifaoui, A. Abdelkrim, and M. Benrejeb. “On the Use of Neural Network as a Universal Approximator”. In: *International Journal of Sciences* 2 (Aug. 2008), pp. 386–399 (cit. on p. 26).
- [47] R. E. Smith, J.-D. Tournier, F. Calamante, and A. Connelly. “SIFT: Spherical-deconvolution informed filtering of tractograms”. In: *Neuroimage* 67 (2013), pp. 298–312 (cit. on p. 35).
- [48] R. E. Smith, J.-D. Tournier, F. Calamante, and A. Connelly. “Anatomically-constrained tractography: Improved diffusion MRI streamlines tractography through effective use of anatomical information”. In: *NeuroImage* 62.3 (2012), pp. 1924–1938. ISSN: 1053-8119. DOI: <https://doi.org/10.1016/j.neuroimage.2012.06.005>. URL: <http://www.sciencedirect.com/science/article/pii/S1053811912005824> (cit. on p. 34).
- [49] O. Sporns. “Brain connectivity”. In: *Scholarpedia* 2.10 (2007). revision #91084, p. 4695. DOI: 10.4249/scholarpedia.4695 (cit. on p. 17).

- [50] O. Sporns. “Graph theory methods: applications in brain networks”. In: *Dialogues in clinical neuroscience* 20.2 (2018), p. 111 (cit. on p. 16).
- [51] O. Sporns and D. S. Bassett. “Editorial: New Trends in Connectomics”. In: *Network Neuroscience* 2.2 (2018), pp. 125–127. DOI: [10.1162/netn\\_e\\_00052](https://doi.org/10.1162/netn_e_00052). eprint: [https://doi.org/10.1162/netn\\_e\\_00052](https://doi.org/10.1162/netn_e_00052). URL: [https://doi.org/10.1162/netn\\_e\\_00052](https://doi.org/10.1162/netn_e_00052) (cit. on p. 17).
- [52] O. Sporns, G. Tononi, and R. Kötter. “The human connectome: a structural description of the human brain”. In: *PLoS Comput Biol* 1.4 (2005), e42 (cit. on p. 16).
- [53] E. O. Stejskal and J. E. Tanner. “Spin diffusion measurements: spin echoes in the presence of a time-dependent field gradient”. In: *The journal of chemical physics* 42.1 (1965), pp. 288–292 (cit. on pp. 9, 11).
- [54] J.-L. R. Stevens, P. Rudiger, and J. A. Bednar. “HoloViews: Building complex visualizations easily for reproducible science”. In: *Proceedings of the 14th Python in Science Conference*. 2015, pp. 61–69 (cit. on p. 42).
- [55] B. Szalkai, B. Varga, and V. Grofusz. “Graph theoretical analysis reveals: Women’s brains are better connected than men’s”. In: *PLoS One* 10.7 (2015), e0130045 (cit. on p. 47).
- [56] P. Tahmasebi, S. Kamrava, T. Bai, and M. Sahimi. “Machine learning in geo- and environmental sciences: From small to large scale”. In: *Advances in Water Resources* 142 (2020), p. 103619. ISSN: 0309-1708. DOI: <https://doi.org/10.1016/j.advwatres.2020.103619>. URL: <http://www.sciencedirect.com/science/article/pii/S0309170820301366> (cit. on p. 25).
- [57] Y. Taki, B. Thyreau, S. Kinomura, K. Sato, R. Goto, R. Kawashima, and H. Fukuda. “Correlations among brain gray matter volumes, age, gender, and hemisphere in healthy individuals”. In: *PloS one* 6.7 (2011), e22734 (cit. on p. 47).
- [58] D. G. Taylor and M. C. Bushell. “The spatial mapping of translational diffusion coefficients by the NMR imaging technique”. In: *Physics in Medicine and Biology* 30.4 (Apr. 1985), pp. 345–349. DOI: [10.1088/0031-9155/30/4/009](https://doi.org/10.1088/0031-9155/30/4/009). URL: <https://doi.org/10.1088%2F0031-9155%2F30%2F4%2F009> (cit. on p. 9).
- [59] K. D. Toennies. *Guide to medical image analysis*. Springer (cit. on p. 9).
- [60] J. Tohka, E. Moradi, H. Huttunen, A. D. N. Initiative, et al. “Comparison of feature selection techniques in machine learning for anatomical brain MRI in dementia”. In: *Neuroinformatics* 14.3 (2016), pp. 279–296 (cit. on p. 18).

- [61] J. D. Tournier, F. Calamante, and A. Connelly. “Improved probabilistic streamlines tractography by 2nd order integration over fibre orientation distributions”. In: *Proceedings of the international society for magnetic resonance in medicine*. Vol. 1670. Ismrm. 2010 (cit. on p. 35).
- [62] J.-D. Tournier, F. Calamante, D. G. Gadian, and A. Connelly. “Direct estimation of the fiber orientation density function from diffusion-weighted MRI data using spherical deconvolution”. In: *Neuroimage* 23.3 (2004), pp. 1176–1185 (cit. on pp. 13, 14).
- [63] J.-D. Tournier, R. Smith, D. Raffelt, R. Tabbara, T. Dhollander, M. Pietsch, D. Christiaens, B. Jeurissen, C.-H. Yeh, and A. Connelly. “MRtrix3: A fast, flexible and open software framework for medical image processing and visualisation”. In: *NeuroImage* 202 (2019), p. 116137 (cit. on pp. 29, 43).
- [64] J.-D. Tournier, F. Calamante, D. G. Gadian, and A. Connelly. “Direct estimation of the fiber orientation density function from diffusion-weighted MRI data using spherical deconvolution”. In: *NeuroImage* 23.3 (2004), pp. 1176–1185. ISSN: 1053-8119. DOI: <https://doi.org/10.1016/j.neuroimage.2004.07.037>. URL: <http://www.sciencedirect.com/science/article/pii/S1053811904004100> (cit. on p. 14).
- [65] D. C. Van Essen and M. F. Glasser. “The human connectome project: progress and prospects”. In: *Cerebrum: the Dana forum on brain science*. Vol. 2016. Dana Foundation. 2016 (cit. on p. 1).
- [66] D. C. Van Essen, K. Ugurbil, E. Auerbach, D. Barch, T. Behrens, R. Bucholz, A. Chang, L. Chen, M. Corbetta, S. W. Curtiss, et al. “The Human Connectome Project: a data acquisition perspective”. In: *Neuroimage* 62.4 (2012), pp. 2222–2231 (cit. on p. 31).
- [67] S. Vieira, W. H. Pinaya, and A. Mechelli. “Using deep learning to investigate the neuroimaging correlates of psychiatric and neurological disorders: Methods and applications”. In: *Neuroscience & Biobehavioral Reviews* 74 (2017), pp. 58–75 (cit. on p. 26).
- [68] J. G. White, E. Southgate, J. N. Thomson, and S. Brenner. “The structure of the nervous system of the nematode *Caenorhabditis elegans*”. In: *Philos Trans R Soc Lond B Biol Sci* 314.1165 (1986), pp. 1–340 (cit. on p. 17).
- [69] R. K. W. Wong, T. C. M. Lee, D. Paul, J. Peng, and A. Disease Neuroimaging Initiative. “Fiber direction estimation, smoothing and tracking in diffusion MRI”. In: *Ann. Appl. Stat.* 10.3 (Sept. 2016), pp. 1137–1156. DOI: 10.1214/15-AOAS880. URL: <https://doi.org/10.1214/15-AOAS880> (cit. on p. 9).
- [70] C.-H. Yeh, D. K. Jones, X. Liang, M. Descoteaux, and A. Connelly. “Mapping Structural Connectivity Using Diffusion MRI: Challenges and Opportunities”. In: *Journal of Magnetic Resonance Imaging* (2020) (cit. on pp. 46, 48).



# Acronyms

5TT	Five Tissue Type
AC-PC	anterior and posterior commissure
ACT	Anatomically Constrained Tractography
ADC	apparent diffusion coefficient
ANN	Artificial Neural Network
API	Application Processing Interface
AUC	area under ROC curve
CSD	Constrained Spherical Deconvolution
CSF	Cerebro-Spinal Fluid
CT	Computed Tomography
dMRI	Diffusion Magnetic Resonance Imaging
DTI	Diffusion Tensor Imaging
DWI	Diffusion Weighted Imaging
FA	fractional anisotropy
fMRI	functional Magnetic Resonance Imaging
fODF	Fiber Orientation Distribution Function
FOV	Field of View
GM	Grey Matter
HARDI	High Angular Resolution Imaging
HCP	Human Connectome Project
MD	mean diffusivity
MEWS	Maximum Edge Weight Subgraph
MIP	Mixed Integer Programming
ML	machine learning

MLP	Multi Layer Perceptron
MRI	Magnetic Resonance Imaging
MWCS	Maximum Weight Connected Subgraph
NMR	Nuclear Magnetic Resonance
PCA	Principal Component Analysis
PDF	probability distribution function
PET	Positron Emission Tomography
PGSE	Pulsed-gradient Spin-echo
RF	radio frequency
RF	Random Forests
RGB	red, green and blue
ROC	Receiver Operator Characteristics
ROI	Region of Interest
SD	Spherical Deconvolution
SE	Single-shot Spin-echo
SIFT	Spherical Informed Filtering
SNR	signal to noise ratio
SVC	Support Vector Classifier
SVM	Support Vector Machines
TE	echo time
TR	repetition time
WM	White Matter

# Acknowledgements

Completing my master's thesis during an ongoing pandemic was a big challenge; both personally and professionally. It was through the constant support of my supervisors, family and friends that I have been able to complete this thesis. First of all, I am very greatful to Prof. Dr. Thomas Schultz for the support and guidance during the course this thesis. His insights have been very valuable for developing a consolidated research plan and viewing the research problem critically. He also made it possible for me to receive a fellowship from the Deutscher Akademiker Austauchdienst (DAAD). I am also very thankful to him for delivering interesting and elucidate courses that sparked my research interests and propelled me to research on this topic.

Secondly, I would like to thank Mohammad Khatami for being my day-to-day supervisor and being very patient with all my questions. He gave me constant feedback and was immensely helpful solve implementational problems. I am also indebted to Dr. Regina Wehler whose Master Thesis Research made it easy for me to get started with my research topic.

I am also thankful to the DAAD and the German Foreign Office (AA) for financially supporting my master's thesis. The financial support made it possible for me maintain my focus during my project.

Data for the project were provided [in part] by the Human Connectome Project, WU-Minn Consortium (Principal Investigators: David Van Essen and Kamil Ugurbil) funded by the 16 NIH Institutes and Centers that support the NIH Blueprint for Neuroscience Research; and by the McDonnell Center for Systems Neuroscience at Washington University.

---

Location, Date

---

Signature



# Declaration of Authorship

I declare that the work presented here is original and the result of my own investigations. Formulations and ideas taken from other sources are cited as such. It has not been submitted, either in part or whole, for a degree at this or any other university.

Location, Date

Signature